TECHNICAL MEMORANDUM

436

RTMIPAS: A fast radiative transfer model for the assimilation of infrared limb radiances from MIPAS

Niels Bormann, Marco Matricardi, and Sean B. Healy

Research Department

April 2004

European Centre for Medium-Range Weather Forecasts
Europäisches Zentrum für mittelfristige Wettervorhersage
Centre européen pour les prévisions météorologiques à moyen terme

Series: ECMWF Technical Memoranda

A full list of ECMWF Publications can be found on our web site under:
http://www.ecmwf.int/publications/

Contact: library@ecmwf.int

European Centre for Medium-Range Weather Forecasts
Shinfield Park, Reading, RG2 9AX, England

Abstract

A new fast radiative transfer model to compute infrared limb radiances for the Michelson Interferometer for Passive Atmospheric Sounding (MIPAS) has been developed and extensively validated. The model, referred to as RTMIPAS, can simulate radiances for all channels of the high-spectral resolution MIPAS instrument in the 685-2000 cm^{-1} wavenumber region (at 0.025 cm^{-1} resolution). RTMIPAS is part of a wider effort to develop the capability to assimilate infrared limb radiances into the ECMWF model. The scheme uses linear regression models to parameterise the effective layer optical depths, and it can simulate the effect of variable water vapour and ozone; contributions for many other gases are included, but a fixed climatological profile is assumed.

The development of the model has involved the calculation of an accurate line-by-line transmittance database, the selection of suitable predictors for the gases and the viewing geometry modelled, and the generation of regression coefficients for 43,205 MIPAS channels.

RTMIPAS can reproduce line-by-line radiances to an accuracy that is below the noise-level of the instrument for most spectral points and tangent heights, while offering significantly more rapid radiance calculations compared to currently available radiative transfer models. The comparison of RTMIPAS transmittances with line-by-line model equivalents indicates that the accuracy of the RTMIPAS transmittance model is comparable to that of similar regression-based radiative transfer models for the nadir viewing geometry.

1 Introduction

This report describes the development and validation of a fast radiative transfer model for limb radiances from the Michelson Interferometer for Passive Atmospheric Sounding (MIPAS, e.g., European Space Agency, ESA, 2000) on-board the Envisat satellite. This is the first step of a wider effort to assimilate infrared limb radiances into a numerical weather prediction (NWP) model. MIPAS is an interferometer with very high spectral resolution (0.025 cm^{-1}, unapodised), measuring infrared limb radiances in 5 spectral bands between 685 and 2410 cm^{-1} (Table 1), providing a total of 59,605 spectral points (i.e., channels). In-flight measurements of the instrument noise are displayed in Fig. 1. MIPAS' main aim is to provide information on the thermal structure and chemical composition of the upper troposphere and the stratosphere at high vertical resolution.

The availability of an appropriate radiative transfer model is a prerequisite for exploiting radiance data from satellite sounders. The radiative transfer model can either be used in a retrieval scheme (e.g., Rodgers 1976), or it can become an "observation operator" in a variational data assimilation scheme (e.g., Eyre et al. 1993). For

Table 1: Main characteristics of MIPAS.

Spectral resolution	0.025 cm^{-1}, unapodised (0.035 cm^{-1}, apodised)		
Spectral bands	A-band:	685-970 cm^{-1}	(11,401 spectral points)
	AB-band:	1020-1170 cm^{-1}	(6,001 spectral points)
	B-band:	1215-1500 cm^{-1}	(11,401 spectral points)
	C-band:	1570-1750 cm^{-1}	(7,201 spectral points)
	D-band:	1820-2410 cm^{-1}	(23,601 spectral points)
Nominal tangent altitudes in normal scanning mode	6-42 km in 3 km steps; 47, 52, 60, 68 km.		
Field of view at tangent point (vertical $\times$ horizontal)	approximately 3 km $\times$ 30 km		

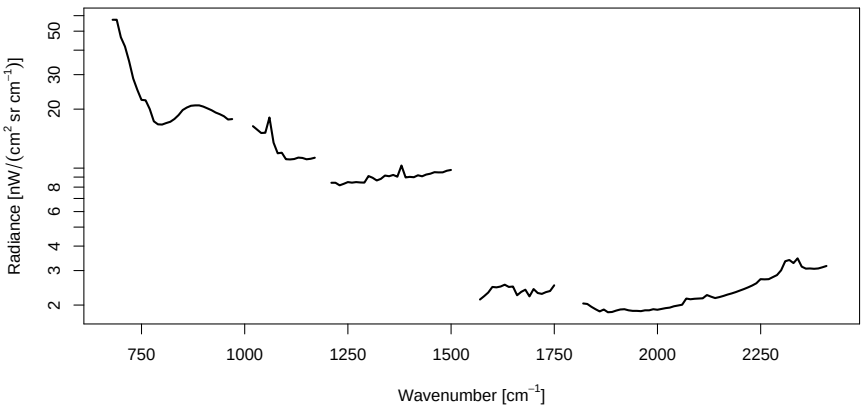

Figure 1: Apodised noise equivalent spectral radiances for MIPAS from the well-studied orbit 2081 (A. Dudhia 2003, pers. communication).

any realtime or near-realtime applications, speed of the radiative transfer model is a major issue.

Fast radiative transfer models used in the assimilation of nadir radiances employ regression-based parameterisations of band-transmittances (e.g., McMillin et al. 1995, Matricardi et al. 2004). One example is RTTOV (or variations of this for advanced nadir sounders, e.g., Matricardi 2003, Matricardi et al. 2004), which uses fixed pressure levels and calculates convolved level-to-space transmittances from each level based on linear regression models for the effective layer optical depths in each layer. The RTTOV approach is used for the direct assimilation of nadir radiances at ECMWF and a number of other NWP centres. Intercomparison studies of various radiative transfer models indicate that nowadays regression-based radiative transfer schemes for nadir sounders agree with line-by-line (LBL) calculations within the variability of different LBL models, and this variability is much smaller than the uncertainties in the spectroscopy (e.g., Garand et al. 2001).

Fast radiative transfer models currently used in retrieval schemes for infrared limb sounders are generally based on the look-up table concept. For instance, Marks and Rodgers (1993) developed an approach based on convolved transmittances pre-tabulated in terms of mass of absorber, mass-weighted pressure, and mass-weighted temperature along the line of sight, which was used for the Improved Stratospheric and Mesospheric Sounder (ISAMS). More recently, the MIPAS community developed radiative transfer models that use look-up tables for the absorption cross sections on irregular spectral grids (e.g., Dudhia et al. 2002b, Ridolfi et al. 2000). In these models, monochromatic radiative transfer calculations are performed only for an optimised sub-set of spectral points. Linear interpolation is then used to obtain monochromatic radiances on the wavenumber grid required for the subsequent convolution with the instrument line shape (ILS). This approach is used in the real-time processing of MIPAS data at ESA to derive profiles of temperature and pressure, as well as mixing ratios for H_2O, O_3, HNO_3, CH_4 and N_2O.[1] However, the complexity of the model and the still considerable execution time make it not suitable for use in an operational variational assimilation scheme.

In this report we describe a regression-based fast radiative transfer model for MIPAS (referred to as "RTMIPAS"). In the current version of the model, only water vapour and ozone are treated as variable gases, but the method could be extended to other gases if required. The structure of this report is as follows: First, we outline the radiative transfer and transmittance parameterisations used in RTMIPAS, with particular emphasis on the limb-specific implementation choices. We then evaluate the performance of the scheme compared to LBL computations. Conclusions are drawn in the last section in which we also discuss the strengths and weaknesses of our approach.

[1] The near-real-time ozone-profile product from MIPAS is currently assimilated operationally at ECMWF (Dethof 2003).

2 Description of the model

2.1 Radiative transfer equation

Given a limb-ray through the atmosphere, characterised by its tangent height z_{tan}, the monochromatic clear-sky radiance $R_\nu(l_{\text{obs}}, z_{\text{tan}})$ for the frequency ν at the observer's position l_{obs} along this ray path can be written as (e.g., Kidder and Vonder Haar 1995):

$$R_\nu(l_{\text{obs}}, z_{\text{tan}}) \;=\; R_\nu(0, z_{\text{tan}})\; \tau_\nu(l_{\text{obs}}, 0, z_{\text{tan}}) + \int_{l=0}^{l_{\text{obs}}} B_\nu(T(l, z_{\text{tan}}))\; \frac{\partial \tau_\nu(l_{\text{obs}}, l, z_{\text{tan}})}{\partial l}\, dl \tag{1}$$

with l denoting the path coordinate along the line of sight, $\tau_\nu(l_1, l_2, z_{\text{tan}})$ the spectral transmittance at wavenumber ν for the path (l_1, l_2) along the ray with tangent height z_{tan}, and $B_\nu(T(l, z_{\text{tan}}))$ the Planck function for the scene temperature T and wavenumber ν. The background space radiance $R_\nu(0, z_{\text{tan}})$ is assumed to be zero for the remainder of this text. This is acceptable if the path origin $l = 0$ is chosen sufficiently outside of the atmosphere on the ray side away from the observer. In the above equation we have assumed local thermodynamic equilibrium and neglected scattering. Note that the path for the path integral is not a straight line, but instead it is affected by refraction in the atmosphere and therefore bends towards the Earth.

The line-of-sight radiance for the MIPAS channel with central wavenumber $\hat{\nu}$ is obtained by convolving the monochromatic radiance with the normalised instrument line shape (ILS) $u_{\hat{\nu}}(\nu)$ to obtain:

$$\hat{R}_{\hat{\nu}}(l_{\text{obs}}, z_{\text{tan}}) \;=\; \int_{\nu=-\infty}^{+\infty} R_\nu(l_{\text{obs}}, z_{\text{tan}})\; u_{\hat{\nu}}(\nu)\, d\nu \tag{2}$$

If the Planck function does not vary too much over the channel response function, equation (1) can be written as:

$$\hat{R}_{\hat{\nu}}(l_{\text{obs}}, z_{\text{tan}}) \approx \int_{l=0}^{l_{\text{obs}}} B_{\hat{\nu}}(T(l, z_{\text{tan}}))\; \frac{\partial \hat{\tau}_{\hat{\nu}}(l_{\text{obs}}, l, z_{\text{tan}})}{\partial l}\, dl \tag{3}$$

$\hat{\tau}_{\hat{\nu}}$ indicates the convolved transmittance for a MIPAS channel with central wavenumber $\hat{\nu}$. Numerical calculations for a number of diverse atmospheric conditions show that the use of convolved quantities in the radiative transfer equation (polychromatic approximation) introduces errors well below the MIPAS noise level.

Finally, convolution in the vertical with the instrument's normalised field of view (FOV) function f gives the FOV radiance $\hat{R}^{FOV}_{\hat{\nu}}(l_{\text{obs}}, z_{\text{tan}})$:

$$\hat{R}^{FOV}_{\hat{\nu}}(l_{\text{obs}}, z_{\text{tan}}) \;=\; \int_{z=0}^{+\infty} \hat{R}_{\hat{\nu}}(l_{\text{obs}}, z)\; f(z - z_{\text{tan}})\, dz \tag{4}$$

2.2 Atmospheric layering and ray-tracing

In RTMIPAS, the radiative transfer integral (3) is solved based on a number of discrete layers. For this purpose, the atmosphere is represented on 81 fixed pressure levels. These pressure levels are given in Table 2 and displayed in Figure 2. The spacing of the levels is similar to that used by Matricardi (2003), and it has been chosen by taking into account typical temperature lapse rates and the expected future vertical discretisation of

the ECMWF forecast model. Additional computations for a range of different atmospheric conditions with a doubled vertical resolution showed that the radiance sensitivity to the pressure grid refinement is well below the noise level of the MIPAS instrument (not shown). The lowest level corresponds to the lowest level typically within the MIPAS FOV, whereas the top has been chosen as a compromise between the (future) top of the ECMWF model atmosphere (at 0.01 hPa) and an even higher top of the atmosphere which would allow modelling the contributions from these mesospheric levels. To investigate the sensitivity of the model to the choice of the top of the model atmosphere we compared simulated radiances calculated with a top of the atmosphere at 120 km with radiances simulated with the top of the atmosphere as used in RTMIPAS (approx. 87 km). The radiance differences were found to be negligible, except in some strong-absorption channels which can be avoided in retrieval or assimilation schemes.

Ray-tracing is required to obtain the ray path and the atmospheric conditions along the path for a given atmospheric state and the satellite's pointing information. Note that in the limb geometry, a given ray will not necessarily cross all the layers introduced in RTMIPAS, and the ones which are crossed are crossed twice

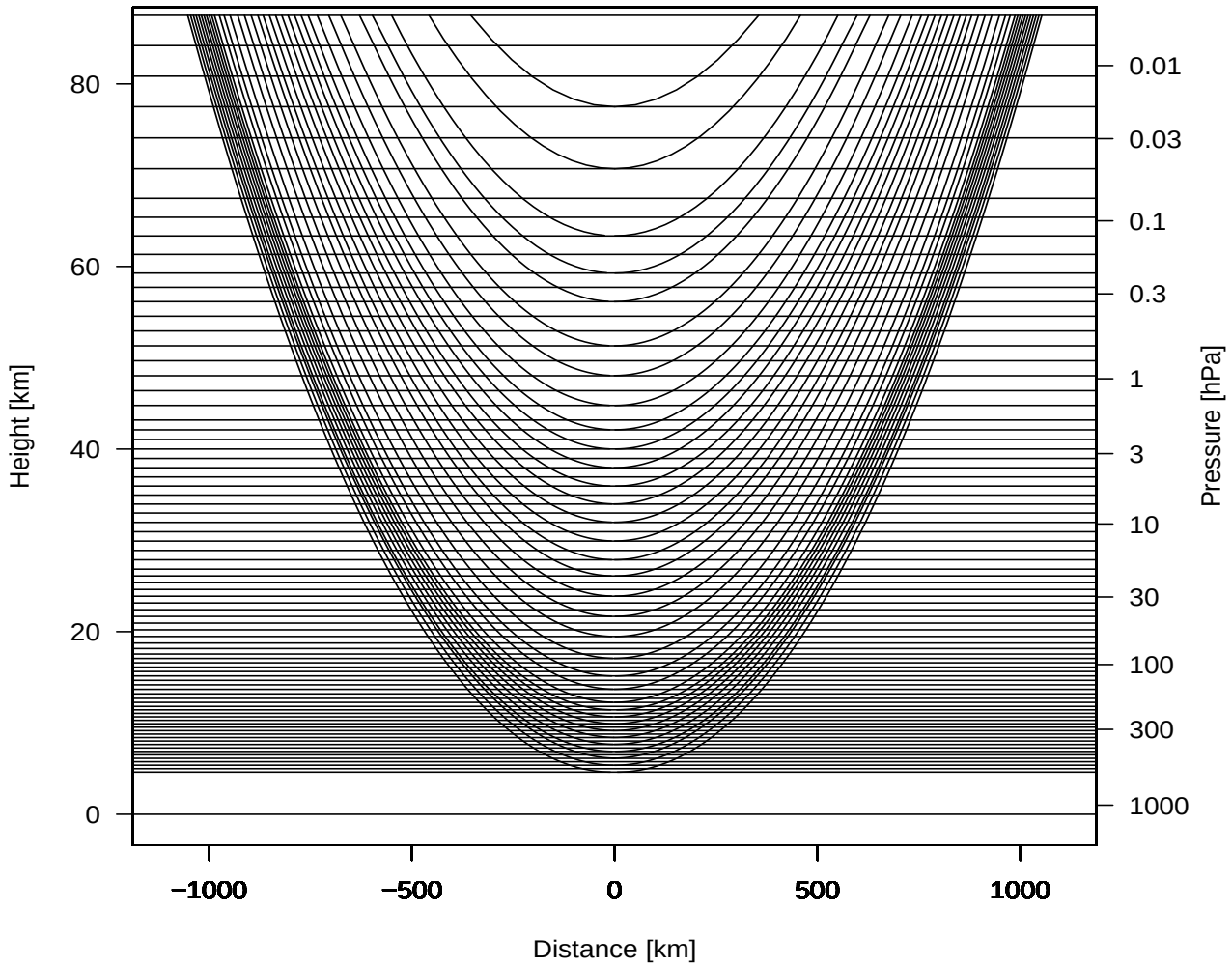

Figure 2: Schematic representation of the levels (horizontal lines) and pencil beams (curved lines) used in RTMIPAS, mapped into a plane-parallel view. An atmospheric mean profile has been used to convert the RTMIPAS pressure levels to heights.

(Fig. 2). In the following, we will use the numbers 1 to 81 to refer to the pressure levels crossed by the ray on the satellite-ward side of the tangent point (with 1 at the top of the atmosphere), and 81 to 161 (counting upwards) to the ones on the other side. This defines a maximum of $N = 160$ layers. The ray tracing is performed using the methods of Healy and Eyre (2003). The result of the ray tracing is mixing ratios of water vapour and ozone at each pressure level crossed by a given ray, as well as path lengths and Curtis Godson air density weighted mean temperatures for each layer (e.g., Ridolfi et al. 2000). For simplicity, we consider only rays whose tangent heights lie on a layer boundary, and use the FOV convolution to calculate the radiances for any other tangent height viewed by MIPAS, as described further below. The hydrostatic equation is used to obtain the geometric height if it is not provided by the user.

Using the atmospheric layering for a ray with the tangent point at the m-th pressure level, equation (3) thus becomes:

$$\hat{R}_{\hat{\nu},m} \approx \sum_{j=1}^{m-1} B_{\hat{\nu}}(T_{j,m}^{CG}) \, (\hat{\tau}_{\hat{\nu},j,m} - \hat{\tau}_{\hat{\nu},j+1,m}) + \sum_{j=N-m+2}^{N} B_{\hat{\nu}}(T_{j,m}^{CG}) \, (\hat{\tau}_{\hat{\nu},j,m} - \hat{\tau}_{\hat{\nu},j+1,m}) \tag{5}$$

Here, $\hat{\tau}_{\hat{\nu},j,m}$ are the convolved transmittances from the j-th level to the observer along the given path. The fast parameterisation of $\hat{\tau}$ is the heart of RTMIPAS, and it will be described in the next subsection. $T_{j,m}^{CG}$ is the Curtis Godson mean temperature of the j-th layer as provided by the ray-tracing, calculated assuming the temperature varies linearly with height between the layer boundaries.

The above calculations are performed for rays with tangent points at a number of levels, spanning the FOVs of the instrument. The choice of the number of such "pencil beams" is a tradeoff between computational cost and accuracy. For RTMIPAS, we found it sufficient to calculate limb radiances only for the tangent points indicated in Table 2, and then evaluate the FOV integral based on a cubic approximation to $\hat{R}_{\hat{\nu}}(l_{\text{obs}}, z_{\text{tan}})$. The FOV function f is assumed to vary linearly with height between the tabulated values. Similar approaches are used in the operational ESA retrieval processing, where a 2nd-order polynomial is used to represent $\hat{R}_{\hat{\nu}}(l_{\text{obs}}, z)$ between the pencil beams for the nominal MIPAS tangent heights (e.g., Ridolfi et al. 2000).

The error introduced by using the chosen subset of pencil beams is difficult and costly to assess, as this requires a very large number of pencil beam radiances to be calculated to obtain a high-resolution radiance versus tangent height relationship. Also, the error depends on the channel, atmospheric condition, and the location of the pencil beams relative to the FOV. To characterise the sensitivity of RTMIPAS to the FOV convolution we compared simulated FOV-convolved MIPAS radiances calculated in two ways: using the 34 pencil beam radiances selected in RTMIPAS, and using all RTMIPAS levels as tangent levels for pencil beam calculations. The computations were performed for the nominal tangent altitudes in the normal scanning mode (Table 1), using the Reference Forward Model (RFM, Dudhia et al. 2002b). The calculations are for five reference profiles, representing mid-latitude daytime, mid-latitude nighttime, polar summer, polar winter, and tropical conditions (John Remedios 2003, pers. communication). Figure 3 shows the noise-normalised maximum absolute radiance difference between the two calculations obtained for the 5 reference profiles. It can be seen that using the sub-set of pencil beams leads to relatively small radiance differences (less than 0.4 times the MIPAS instrument noise) for most channels and tangent heights, except for the lowest tangent height at 6 km, where the differences can exceed the MIPAS noise level. The larger deviations for the 6 km tangent height occur for the tropical profile for which the tangent height for the lowest pencil beam is too high to fully capture the radiance profile within the FOV, and extrapolation is used. While the FOV calculations summarised in Fig. 3 do not rule out that the chosen approach for the FOV convolution can introduce more significant errors (particularly in regions of strong curvature of the radiance profile with tangent height), they provide some evidence that the RTMIPAS FOV convolution is not problematic as long as the RTMIPAS pencil beams cover the MIPAS FOV. In any case, it should be stressed that the design of a suitable cost-efficient approach to FOV convolution based on a limited number of pencil beams is not specific to RTMIPAS, and FOV-convolution has been recognised as a possible source of error for other models by other authors (e.g., von Clarmann et al. 2003).

Table 2: Pressure levels used to discretise the atmosphere in RTMIPAS. To give an indication of the corresponding heights these have been calculated from a mean atmospheric profile. The levels for which pencil beam calculations are performed are marked by ticks in the column "Tangent?".

Number	Pressure [hPa]	Height [km]	Tangent?	Number	Pressure [hPa]	Height [km]	Tangent?
1	0.00374	87.5		42	33.3601	23.1	
2	0.00628	84.2		43	37.4579	22.4	
3	0.01050	80.9		44	42.0767	21.7	√
4	0.01724	77.5	√	45	47.2900	20.9	
5	0.02804	74.1		46	53.1713	20.2	
6	0.04469	70.7	√	47	59.7964	19.5	√
7	0.07008	67.5		48	67.2557	18.8	
8	0.09408	65.4		49	74.1827	18.2	
9	0.12532	63.3	√	50	81.8231	17.6	
10	0.16567	61.3		51	88.5000	17.1	√
11	0.21900	59.3	√	52	95.7066	16.6	
12	0.27021	57.7		53	103.500	16.1	
13	0.33340	56.1	√	54	111.955	15.6	
14	0.41136	54.6		55	121.100	15.2	√
15	0.50754	52.9		56	130.996	14.7	
16	0.62623	51.3	√	57	141.700	14.2	
17	0.77266	49.7		58	153.277	13.7	√
18	0.95334	48.0	√	59	165.800	13.2	
19	1.17626	46.4		60	179.347	12.7	
20	1.45131	44.8	√	61	192.105	12.3	√
21	1.79068	43.2		62	205.772	11.8	
22	2.06631	42.1	√	63	218.258	11.4	√
23	2.38435	41.1		64	231.435	11.1	
24	2.75136	40.0	√	65	245.265	10.7	√
25	3.17485	39.0		66	259.922	10.3	
26	3.66352	38.0	√	67	275.152	9.9	√
27	4.22741	37.0		68	291.113	9.5	
28	4.87810	36.0	√	69	308.000	9.2	√
29	5.62894	35.0		70	325.362	8.8	
30	6.49536	34.0	√	71	343.702	8.4	√
31	7.49513	33.0		72	362.907	8.0	
32	8.71793	32.0	√	73	382.828	7.6	√
33	10.1491	31.0		74	403.842	7.3	
34	11.8257	30.0	√	75	425.591	6.9	√
35	13.7913	28.9		76	448.290	6.5	
36	16.0979	27.9	√	77	472.200	6.1	√
37	18.8067	26.9		78	496.738	5.8	
38	21.0782	26.1	√	79	522.551	5.4	√
39	23.6241	25.4		80	549.473	5.0	
40	26.4874	24.6		81	577.297	4.6	√
41	29.7200	23.9	√				

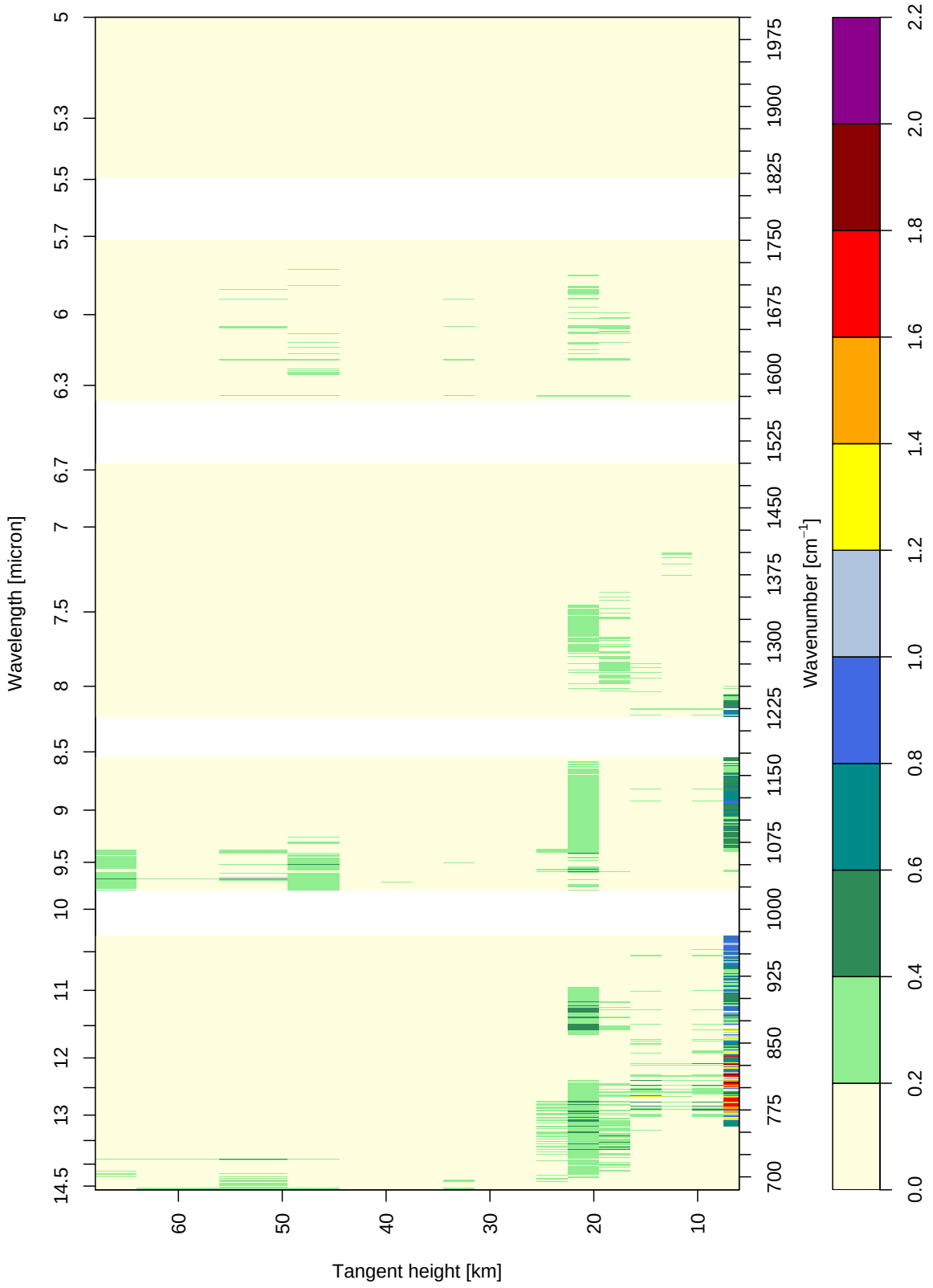

Figure 3: Maximum absolute radiance difference (of 5 profiles) between FOV-convolved simulated MIPAS radiances calculated in the two ways described in the main text. The radiance differences have been normalised by the MIPAS instrument noise, and are shown as a function of wavenumber and central tangent height. For display reasons, the plot shows the maximum of 40 channel intervals (i.e., 1 cm^{-1} intervals).

2.3 Transmittance parameterisation

In the RTMIPAS transmittance calculations only water vapour and ozone are treated as variable gases, whereas the other gases are considered as fixed. The model treats separately the absorption of the fixed gases, water vapour, and ozone to obtain the total transmittance $\hat{\tau}^{\text{fix+H2O+O3}}_{\hat{\nu},j,m}$. Calculation of the total transmittances is complicated by the fact that Beer's law (e.g., Kidder and Vonder Haar 1995) does not apply for polychromatic transmittances, i.e., the product of the transmittances from each of the gases convolved separately is not the same as the convolved transmittance for all gases (except for continuum-like effects). To reduce the errors introduced by separation of the gas transmittances after their convolution we write the total transmittance $\hat{\tau}^{\text{fix+H2O+O3}}_{\hat{\nu},j,m}$ as:

$$\hat{\tau}^{\text{fix+H2O+O3}}_{\hat{\nu},j,m} = \hat{\tau}^{\text{fix}}_{\hat{\nu},j,m} \frac{\hat{\tau}^{\text{fix+H2O}}_{\hat{\nu},j,m}}{\hat{\tau}^{\text{fix}}_{\hat{\nu},j,m}} \frac{\hat{\tau}^{\text{fix+H2O+O3}}_{\hat{\nu},j,m}}{\hat{\tau}^{\text{fix+H2O}}_{\hat{\nu},j,m}} \tag{6}$$

where the superscripts indicate which gases are considered in each transmittance calculation. The three factors on the right hand side thus serve as "effective level-to-satellite transmittances" for the fixed gases, water vapour, and ozone, respectively. We can now introduce convolved effective layer optical depths as:

$$\hat{\sigma}^{\text{fix}}_{\hat{\nu},j,m} - \hat{\sigma}^{\text{fix}}_{\hat{\nu},j-1,m} = -\log\left(\hat{\tau}^{\text{fix}}_{\hat{\nu},j,m} / \hat{\tau}^{\text{fix}}_{\hat{\nu},j-1,m}\right) \tag{7}$$

$$\hat{\sigma}^{\text{H2O}}_{\hat{\nu},j,m} - \hat{\sigma}^{\text{H2O}}_{\hat{\nu},j-1,m} = -\log\left(\frac{\hat{\tau}^{\text{fix+H2O}}_{\hat{\nu},j,m}}{\hat{\tau}^{\text{fix}}_{\hat{\nu},j,m}} / \frac{\hat{\tau}^{\text{fix+H2O}}_{\hat{\nu},j-1,m}}{\hat{\tau}^{\text{fix}}_{\hat{\nu},j-1,m}}\right) \tag{8}$$

$$\hat{\sigma}^{\text{O3}}_{\hat{\nu},j,m} - \hat{\sigma}^{\text{O3}}_{\hat{\nu},j-1,m} = -\log\left(\frac{\hat{\tau}^{\text{fix+H2O+O3}}_{\hat{\nu},j,m}}{\hat{\tau}^{\text{fix+H2O}}_{\hat{\nu},j,m}} / \frac{\hat{\tau}^{\text{fix+H2O+O3}}_{\hat{\nu},j-1,m}}{\hat{\tau}^{\text{fix+H2O}}_{\hat{\nu},j-1,m}}\right) \tag{9}$$

where $\hat{\sigma}_{\hat{\nu},j,m} = -log(\tau_{\hat{\nu},j,m})$ is the convolved level-to-satellite optical depth from level j along the path with tangent height at the level m, and the superscript indicates the relevant gas.

The transmittance parameterisation in RTMIPAS is based on regression models for the above convolved effective layer optical depths, following algorithms that have been developed over the years for a number of different satellite instruments (McMillin et al. 1979, Susskind et al. 1983, Eyre 1991, Strow et al. 2003). The convolved level-to-satellite optical depths are written as:

$$\hat{\sigma}_{\hat{\nu},j,m} = \hat{\sigma}_{\hat{\nu},j-1,m} + \sum_{k=1}^{M} a_{\hat{\nu},j,k}\, x_{j,k} \tag{10}$$

where $x_{j,k}$ are profile dependent predictors characterising the atmospheric state along the ray, M is the number of predictors, and $a_{\hat{\nu},j,k}$ are the regression coefficients for each layer. Regression coefficients are computed for the fixed gases, ozone, water vapour line absorption, and water vapour continuum absorption, respectively. To compute the regression coefficients, we generated databases of accurate LBL transmittances for a set of diverse profiles which represent the atmospheric variability across the MIPAS viewing range (see section 2.4 for details). The effective optical depths from this database are then used to compute the regression coefficients by linear regression of $\hat{\sigma}_{\hat{\nu},j,m} - \hat{\sigma}_{\hat{\nu},j-1,m}$ versus the predictor values calculated from the profile variables. A separate model is used for the water vapour continuum absorption. This allows to update the model for the continuum absorption without the need of generating a new LBL database. Since the continuum-type optical depths vary very slowly with frequency, the convolved optical depths can be replaced by monochromatic calculations.

The predictors used in this report are given in Table 4, with the profile variables defined in Table 3. The predictors are originally based on Matricardi et al. (2004), with modifications for the limb geometry. Given the different viewing geometry, a necessary adjustment to the predictors was to replace the secant of the satellite

zenith angle with the actual layer path length ($\Delta\tilde{s}$). All predictors are defined by taking the ratio with respect to values of a reference profile or a typical value (in the case of the layer path length), to avoid numerical instabilities in the regressions due to too large variation in the predictors. For the fixed gases, the predictors depend only on the temperature along the path and the layer path length, whereas for the variable gases the variation in the absorber amount has to be taken into account. The layer optical depth is expected to be proportional to the absorber amount n for weak absorption and $\sqrt{n}$ for strong absorption (Goody and Yung 1995), which is reflected in the more basic predictors. Combined effects of weak and strong absorption are modelled through further variations in the exponent. Similar to Matricardi et al. (2004) we found it necessary to take into account the dependence of the layer optical depth on the properties along the ray path towards the satellite, even though the ratioing introduced in (6) reduces this dependence. Further details on the choice of predictors can be found in Matricardi et al. (2004), and our set of predictors is further characterised statistically in section 2.5. From Table 4 it can be seen that the water vapour continuum model uses predictors that depend on Curtis-Godson air density weighted mean values. This was found to give better results rather than using the simple arithmetic average of the values at the top and bottom of the layer. Note that the water vapour continuum model predicts monochromatic optical depths so that the predictors depend only on layer average quantities and not, as in the case of the polychromatic optical depths, on quantities integrated along the ray path towards the satellite.

Similar to the approach taken in Matricardi (2003), we found it beneficial to perform a weighted regression where the layer optical depths have weights given by $\hat{\tau}_{\hat{\nu},j,m}\ \hat{\tau}_{\hat{\nu},j+1,m}$. This is particularly advantageous for channels which, in some layers, exhibit changes in the behaviour of the layer optical depth against some predictors for strong attenuation cases, such as some water vapour channels for which layer optical depths can start to decrease with $\Delta\tilde{s}\,\tilde{W}_r$ when the attenuation along the ray towards the satellite is strong (cf, Matricardi and Saunders 1999). The weighting used assures that the regression model is primarily influenced by the linear regime of the weakly attenuated cases. The behaviour of the regression model for the cases with strong attenuation along the ray towards the satellite is of little importance, as larger errors in the layer optical depth translate to small errors in terms of transmittances for these cases. In addition, the chosen weighting downweights the influence of layer optical depths with numerical inaccuracies resulting from ratioing small level-to-satellite transmittances.

Table 3: Profile variables used to specify the RTMIPAS predictors. In the following, $P(i)$, $T(i)$, $W(i)$, and $O(i)$ are pressure, temperature, water vapour mixing ratio, and ozone mixing ratio on the i-th model level, respectively. A star (*) indicates the reference profile used to scale the profile values. A tilde ($\tilde{}$) indicates that the quantity is defined per layer (rather than level). $\Delta\tilde{s}(i,m)$ represents the scaled path length in the i-th layer for a ray with a tangent point at level m. Similarly, $\Delta\tilde{z}^\star(i)$ represents the scaled geometric depth of the i-th layer for the reference profile.

$$\tilde{T}(j) = \frac{1}{2}\big(T(j+1)+T(j)\big), \qquad \tilde{T}^\star(j) = \frac{1}{2}\big(T^\star(j+1)+T^\star(j)\big), \qquad \tilde{T}_r(j) = \frac{\tilde{T}(j)}{\tilde{T}^\star(j)}$$

$$\tilde{W}(j) = \frac{1}{2}\big(W(j+1)+W(j)\big), \qquad \tilde{W}^\star(j) = \frac{1}{2}\big(W^\star(j+1)+W^\star(j)\big), \qquad \tilde{W}_r(j) = \frac{\tilde{W}(j)}{\tilde{W}^\star(j)}$$

$$\tilde{O}(j) = \frac{1}{2}\big(O(j+1)+O(j)\big), \qquad \tilde{O}^\star(j) = \frac{1}{2}\big(O^\star(j+1)+O^\star(j)\big), \qquad \tilde{O}_r(j) = \frac{\tilde{O}(j)}{\tilde{O}^\star(j)}$$

$$\tilde{T}_w(j,m) = \begin{cases} \dfrac{\sum_{i=1}^{j} P(i)\,\Delta\tilde{s}(i,m)\,\tilde{T}(i)}{\sum_{i=1}^{j} P(i)\,\Delta\tilde{z}^\star(i)\,\tilde{T}^\star(i)} & \text{if } j < m; \\ \dfrac{\sum_{i=1}^{m-1} P(i)\,\Delta\tilde{s}(i,m)\,\tilde{T}(i) + \sum_{i=161-m}^{j} P(i)\,\Delta\tilde{s}(i,m)\,\tilde{T}(i)}{\sum_{i=1}^{m-1} P(i)\,\Delta\tilde{z}^\star(i)\,\tilde{T}^\star(i) + \sum_{i=161-m}^{j} P(i)\,\Delta\tilde{z}^\star(i)\,\tilde{T}^\star(i)} & \text{otherwise.} \end{cases}$$

$$\tilde{W}_w(j,m) = \begin{cases} \dfrac{\sum_{i=1}^{j} P(i)\,\Delta\tilde{s}(i,m)\,\tilde{W}(i)}{\sum_{i=1}^{j} P(i)\,\Delta\tilde{z}^\star(i)\,\tilde{W}^\star(i)} & \text{if } j < m; \\ \dfrac{\sum_{i=1}^{m-1} P(i)\,\Delta\tilde{s}(i,m)\,\tilde{W}(i) + \sum_{i=161-m}^{j} P(i)\,\Delta\tilde{s}(i,m)\,\tilde{W}(i)}{\sum_{i=1}^{j} P(i)\,\Delta\tilde{z}^\star(i)\,\tilde{W}^\star(i)} & \text{otherwise.} \end{cases}$$

$$\tilde{W}_{tw}(j,m) = \begin{cases} \dfrac{\sum_{i=1}^{j} P(i)\,\Delta\tilde{s}(i,m)\,\tilde{T}(i)\,\tilde{W}(i)}{\sum_{i=1}^{j} P(i)\,\Delta\tilde{z}^\star(i)\,\tilde{T}^\star(i)\,\tilde{W}^\star(i)} & \text{if } j < m; \\ \dfrac{\sum_{i=1}^{m-1} P(i)\,\Delta\tilde{s}(i,m)\,\tilde{T}(i)\,\tilde{W}(i) + \sum_{i=161-m}^{j} P(i)\,\Delta\tilde{s}(i,m)\,\tilde{T}(i)\,\tilde{W}(i)}{\sum_{i=1}^{j} P(i)\,\Delta\tilde{z}^\star(i)\,\tilde{T}^\star(i)\,\tilde{W}^\star(i)} & \text{otherwise.} \end{cases}$$

$\tilde{O}_w(j,m)$ and $\tilde{O}_{tw}(j,m)$ defined as $\tilde{W}_w(j,m)$ and $\tilde{W}_{tw}(j,m)$, but for water vapour.

$\tilde{T}_r^{\mathrm{CG}}(j)$ and $\tilde{W}_r^{\mathrm{CG}}(j)$ are the density-weighted Curtis Godson temperature and water vapour mixing ratio, respectively, both obtained from the ray-tracing.

Table 4: Predictors used in RTMIPAS. See Table 3 for a definition of the profile variables used. The predictors are defined per layer j and pencil beam with tangent point at level m; indices such as (j) in $\tilde{T}_r(j)$ and (j,m) in $\Delta\tilde{s}(j,m)$ have been omitted for clarity.

Predictor number	Fixed gases	Water vapour (line)	Ozone	Water vapour (continuum)
1	$\Delta\tilde{s}$	$\Delta\tilde{s}\,\tilde{W}_r$	$\Delta\tilde{s}\,\tilde{O}_r$	$\Delta\tilde{s}\,\tilde{W}_r^{CG}/\tilde{T}_r^{CG}$
2	$\Delta\tilde{s}^2$	$\Delta\tilde{s}\,\tilde{W}_r\,\tilde{T}_r$	$\Delta\tilde{s}\,\tilde{O}_r\,\tilde{T}_r$	$\Delta\tilde{s}\,\tilde{W}_r^{CG}/(\tilde{T}_r^{CG})^2$
3	$\Delta\tilde{s}\,\tilde{T}_r$	$\Delta\tilde{s}\,\tilde{W}_r\,\tilde{T}_r^2$	$\Delta\tilde{s}\,\tilde{O}_r\,\tilde{T}_r^2$	$\Delta\tilde{s}\,(\tilde{W}_r^{CG})^2/\tilde{T}_r^{CG}$
4	$\Delta\tilde{s}\,\tilde{T}_r^2$	$\Delta\tilde{s}\,\tilde{W}_r/\sqrt{\tilde{W}_w}$	$\Delta\tilde{s}\,\tilde{O}_r/\sqrt{\tilde{O}_w}$	$\Delta\tilde{s}\,(\tilde{W}_r^{CG})^2/(\tilde{T}_r^{CG})^4$
5	$\Delta\tilde{s}\,\tilde{T}_r^3$	$\Delta\tilde{s}\,\tilde{W}_r\,\sqrt{\tilde{W}_w}$	$\Delta\tilde{s}\,\tilde{O}_r\,\sqrt{\tilde{O}_w}$	
6	$\Delta\tilde{s}\,\tilde{T}_r^4$	$\sqrt{\Delta\tilde{s}\,\tilde{W}_r}$	$\sqrt{\Delta\tilde{s}\,\tilde{O}_r}$	
7	$\Delta\tilde{s}^{\frac{3}{2}}\,\sqrt{\tilde{T}_r}$	$\sqrt{\Delta\tilde{s}\,\tilde{W}_r}\,\tilde{T}_r$	$\sqrt{\Delta\tilde{s}\,\tilde{O}_r}\,\tilde{T}_r$	
8	$\tilde{T}_r$	$\sqrt{\Delta\tilde{s}\,\tilde{W}_r}/\sqrt{\tilde{W}_w}$	$(\Delta\tilde{s}\,\tilde{O}_r)^{1.5}/\sqrt{\tilde{O}_w}$	
9	$\tilde{T}_r^2$	$\sqrt{\Delta\tilde{s}\,\tilde{W}_r}\,\sqrt{\tilde{W}_{tw}}$	$\sqrt{\tilde{O}_{tw}}$	
10	$\tilde{T}_w$	$(\Delta\tilde{s}\,\tilde{W}_r)^2$	$\tilde{O}_{tw}^2$	
11	$\tilde{T}_w^2$	$\sqrt{\tilde{W}_w}$	$\sqrt{\tilde{O}_w}$	
12		$\tilde{W}_w^2$	$\tilde{O}_w^2$	
13			$\Delta\tilde{s}\,\tilde{T}_r^3$	

2.4 Transmittance database

The transmittance database used to derive the regression coefficients for RTMIPAS was generated using the RFM (Dudhia et al. 2002b), a multi-purpose LBL radiative transfer model originally based on GENLN2 (Edwards 1992). The RFM has been considerably validated and compares favourably with a number of other LBL models for limb viewing (e.g., von Clarmann et al. 2003). Line data were taken from the 2000 edition of the HITRAN molecular database. The fixed gases include all gases with contributions at or above the noise level of the MIPAS instrument, as determined by limb calculations for a reference atmosphere. These are: CO_2, N_2O, CO, CH_4, O_2, NO, SO_2, NO_2, NH_3, HNO_3, OCS, HOCl, N_2, HCN, CH_3Cl, H_2O_2, C_2H_2, C_2H_6, COF_2, SF_6, $ClONO_2$, NO_+, $CFCl_3$ (F11), CF_2Cl_2 (F12), CF_4 (F14), $CHClF_2$ (F22), $C_2Cl_3F_3$ (F113), $C_2Cl_2F_4$ (F114), C_2ClF_5 (F115), CCl_4, N_2O_5, HNO_4. Because of the longer paths, a large number of minor species have to be included in the LBL computation for the limb geometry compared to nadir viewing. Climatological profiles for these species have been used (John Remedios 2003, pers. communication). Where appropriate, the gas concentrations were scaled to expected values for the year 2005, the expected year for assimilation experiments with MIPAS radiances. Sub-Lorentzian wings of CO_2 line shapes have been represented through so-called chi-factor corrections (Cousin et al. 1985, Le Doucen et al. 1985). The continuum type absorption for N_2, O_2 and CO_2 is included (Lafferty et al. 1996, Thibault et al. 1997, Clough et al. 1989). To compute the regression coefficients for the water vapour continuum, a separate database has been generated using the CKD

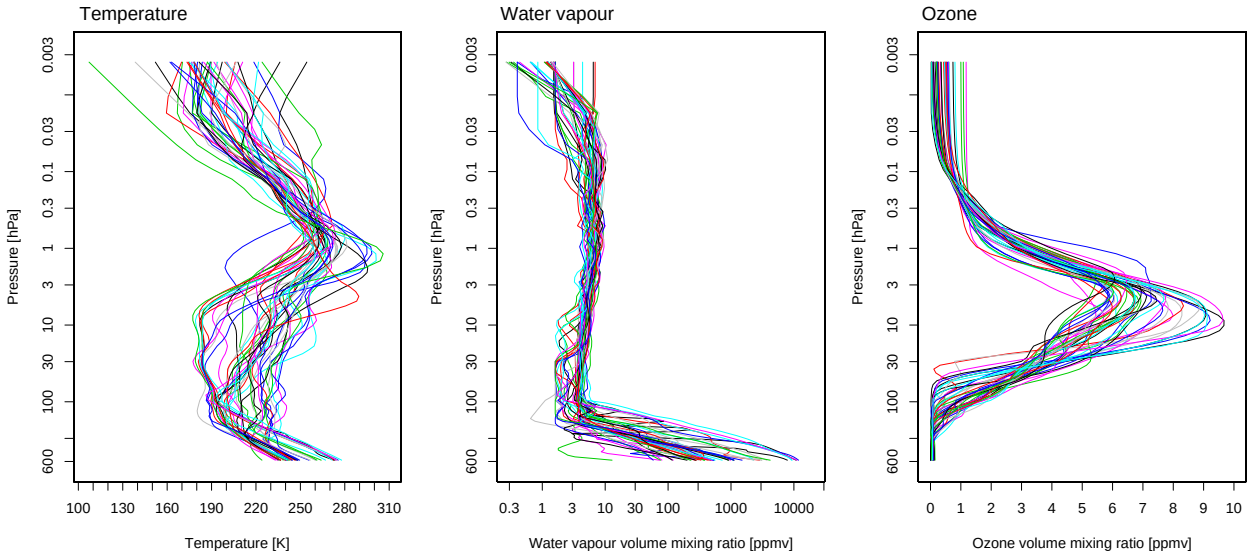

Figure 4: Temperature, water vapour, and ozone mixing ratio profiles of the 46 profile training dataset.

2.4 continuum model (Clough et al. 1989). Monochromatic LBL calculations were performed at a resolution of 0.0005 cm^{-1}. These high-resolution spectra were subsequently convolved with the MIPAS ILSs, apodised using Norton-Beer strong apodisation (Didem Alpaslan and Rob Koopmann 2003, pers. communication). The resolution of 0.0005cm^{-1} wavenumbers is considered sufficient to resolve the sharp Doppler-broadened lines at high altitudes for the limb geometry (e.g., Ridolfi et al. 2000). To confirm this, we computed convolved radiances based on monochromatic calculations with a resolution of 0.001 cm^{-1} and 0.0001 cm^{-1} wavenumbers for some reference profiles. While considerable differences in the convolved radiances were found when moving from the 0.001 cm^{-1} to the 0.0005cm^{-1} resolution, decreasing the resolution further led only to negligible radiance differences. Note that we consider only MIPAS channels in the wavenumber range 685-2000 cm^{-1}, as the channels in the 2000-2410 cm^{-1} region of the spectrum are contaminated by solar radiation and also show poor signal-to-noise characteristics.

The LBL computations are performed for a set of 46 diverse atmospheric profiles (Fig. 4), assuming horizontal homogeneity in the calculations. The profiles are taken from the 60 level ERA-40 reanalysis (e.g., Simmons and Gibson 2000), and provide thermodynamically consistent values of pressure, temperature, and mixing ratios for water vapour and ozone. The profiles were sampled using the method of Chevallier (2002), maximising the variability in the stratosphere and upper troposphere above 550 hPa. For each of the profiles, the required level-to-satellite transmittances and radiances were calculated for a set of limb rays with the tangent points at the pressure levels indicated in Table 2.

The calculation of the transmittance database presents a huge computational effort, leading to a database of about 45 Gbytes per profile for the monochromatic transmittances alone. This computational effort obviously imposes a practical limitation not only on the number of profiles used in the training of the fast transmittance model but also on the number of pencil beams being considered. The number of profiles used in the training set is comparable to that typically used in the derivation of regression coefficients for fast models for the nadir viewing geometry, such as in Matricardi (2003). Since the profiles used in these fast models have to capture the tropospheric as well as the stratospheric variability and because of the intrinsic lower stratospheric variability, we expect that 46 profiles should be adequate for this study.

2.5 Characterisation of the predictor selection

To characterise our predictor selection we investigated the relevance of each predictor through stepwise selection for a subset of channels and layers, in line with methods suggested by Sherlock (2002). Note that there are likely to be non-zero correlations between some predictors, and these potentially limit the accuracy of the estimates for the regression coefficients for a given training dataset. The stepwise selection is based on the training database of effective layer optical depths, using the predictors given in Table 4. Forward selection and backward elimination is based on Akaike's Information Criterion (AIC[2]), which measures the likelihood of the regression model with an additional penalty for the rank of the model (e.g., Venables and Ripley 2002). It should be noted that for simplicity RTMIPAS uses a predictor set that is suitable for all channels and all layers, thus having to cater for a range of different regimes.

Figures 5 to 7 provide examples of the results for the stepwise selection for the fixed gases, water vapour line absorption, and ozone, respectively, each in the MIPAS band in which they are most prominent. The Figures show the percentage of channels for which each predictor was chosen, and the average ranking of each predictor in case it was chosen. For computational reasons we performed the selection only for every 20th channel and every 4th layer.

The results show that all predictors are selected for at least 60 % of the channels in at least one layer, and no predictor appears obviously redundant. This reflects the relevant contribution of all predictors to the transmittance model. For the lower layers (layer numbers around 80), fewer predictors tend to be chosen, as seen in the lower values of the percentage chosen. This may indicate some degree of overfitting in our models for these layers, resulting from the lower number of cases, as only cases from the lowest pencil beams are available. For the fixed gases and ozone, the statistics for each predictor show considerable consistency with layer number, whereas for the water vapour model this is less evident. As expected, given the ratioing introduced in (6), predictors describing layer quantities tend to be selected first, before predictors that characterise the atmosphere on the path towards the satellite. Note, however, that some of these path-weighted predictors are chosen very frequently, despite having a lower average ranking (e.g., $\tilde{T}_w^2$, $\sqrt{\tilde{W}_w}$, $\tilde{O}_{tw}^2$, $\sqrt{\tilde{O}_w}$), indicating the significant additional information these predictors provide. The stepwise selection also shows how the leading predictors for the ozone or water vapour line absorption tend to be proportional to $\Delta\tilde{s}\,\tilde{O}_r$ or $\Delta\tilde{s}\,\tilde{W}_r$ and thus proportional to the layer absorber amount. This behaviour is typical for weak absorption regimes. For the ozone model, strong absorption predictors (proportional to the square root of the absorber amount) become more important around layer 30, i.e., around the ozone maximum. It should be noted as well, that neither the percentage chosen nor the average ranking is a good indicator for predictors which are important for specific regimes represented in a small number of channels. We found this is particularly the case for the model for water vapour line absorption, for which some of the lesser chosen or lower ranked predictors nevertheless add prominent skill for some channels (e.g., $\sqrt{\Delta\tilde{s}\,\tilde{W}_r}$).

[2] AIC$= log(\sigma^2) + 2\frac{M+1}{n}$, with the mean residual variance σ^2, the number of predictors M, and the number of cases n

a) Percentage chosen

Predictor
$\Delta\tilde{s}$
$\Delta\tilde{s}^2$
$\Delta\tilde{s}\,\tilde{T}_r$
$\Delta\tilde{s}\,\tilde{T}_r^2$
$\Delta\tilde{s}\,\tilde{T}_r^3$
$\Delta\tilde{s}\,\tilde{T}_r^4$
$\Delta\tilde{s}^{\frac{3}{2}}\sqrt{\tilde{T}_r}$
$\tilde{T}_r$
$\tilde{T}_r^2$
$\tilde{T}_w$
$\tilde{T}_w^2$

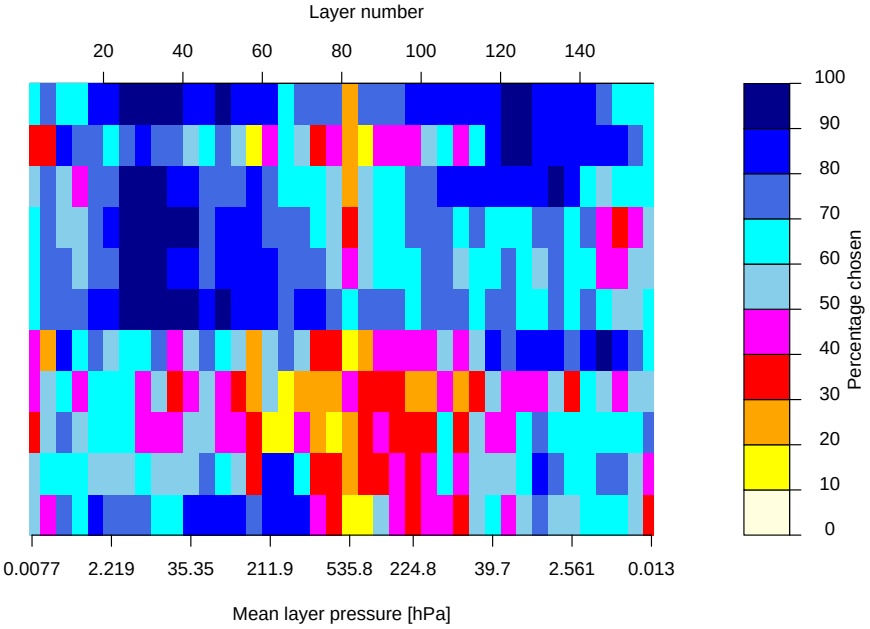

b) Average ranking

Predictor
$\Delta\tilde{s}$
$\Delta\tilde{s}^2$
$\Delta\tilde{s}\,\tilde{T}_r$
$\Delta\tilde{s}\,\tilde{T}_r^2$
$\Delta\tilde{s}\,\tilde{T}_r^3$
$\Delta\tilde{s}\,\tilde{T}_r^4$
$\Delta\tilde{s}^{\frac{3}{2}}\sqrt{\tilde{T}_r}$
$\tilde{T}_r$
$\tilde{T}_r^2$
$\tilde{T}_w$
$\tilde{T}_w^2$

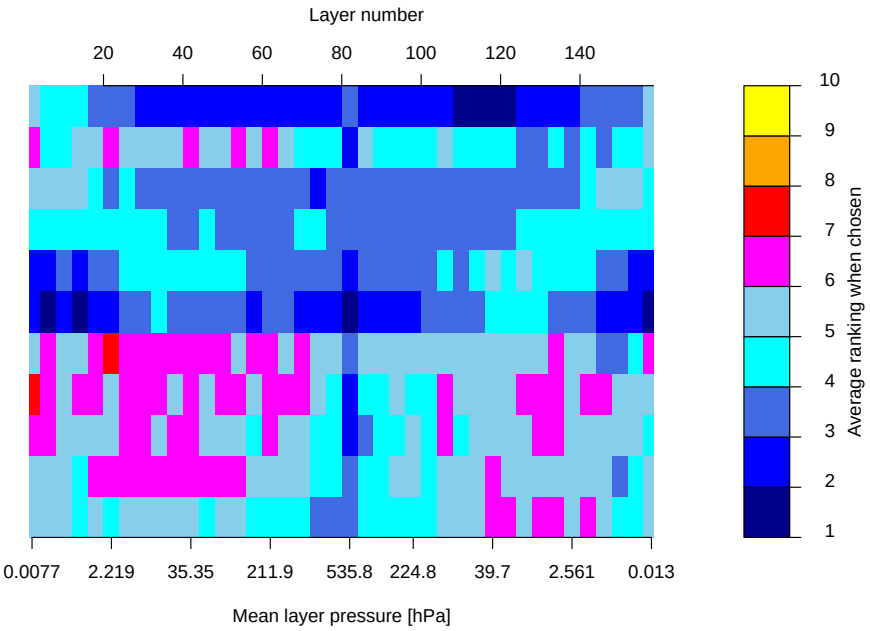

Figure 5: Results of the stepwise selection for the predictors used in the fixed-gases model in RTMIPAS. The plots show (a) the percentage of channels for which the predictor was chosen, and (b) the average ranking when it was chosen for each predictor (listed on the x-axis) as a function of RTMIPAS layer. The stepwise selection is further described in the main text, and it was based on every 20th channel and every 4th layer for the MIPAS A-band. See Table 3 for a definition of the profile variables used.

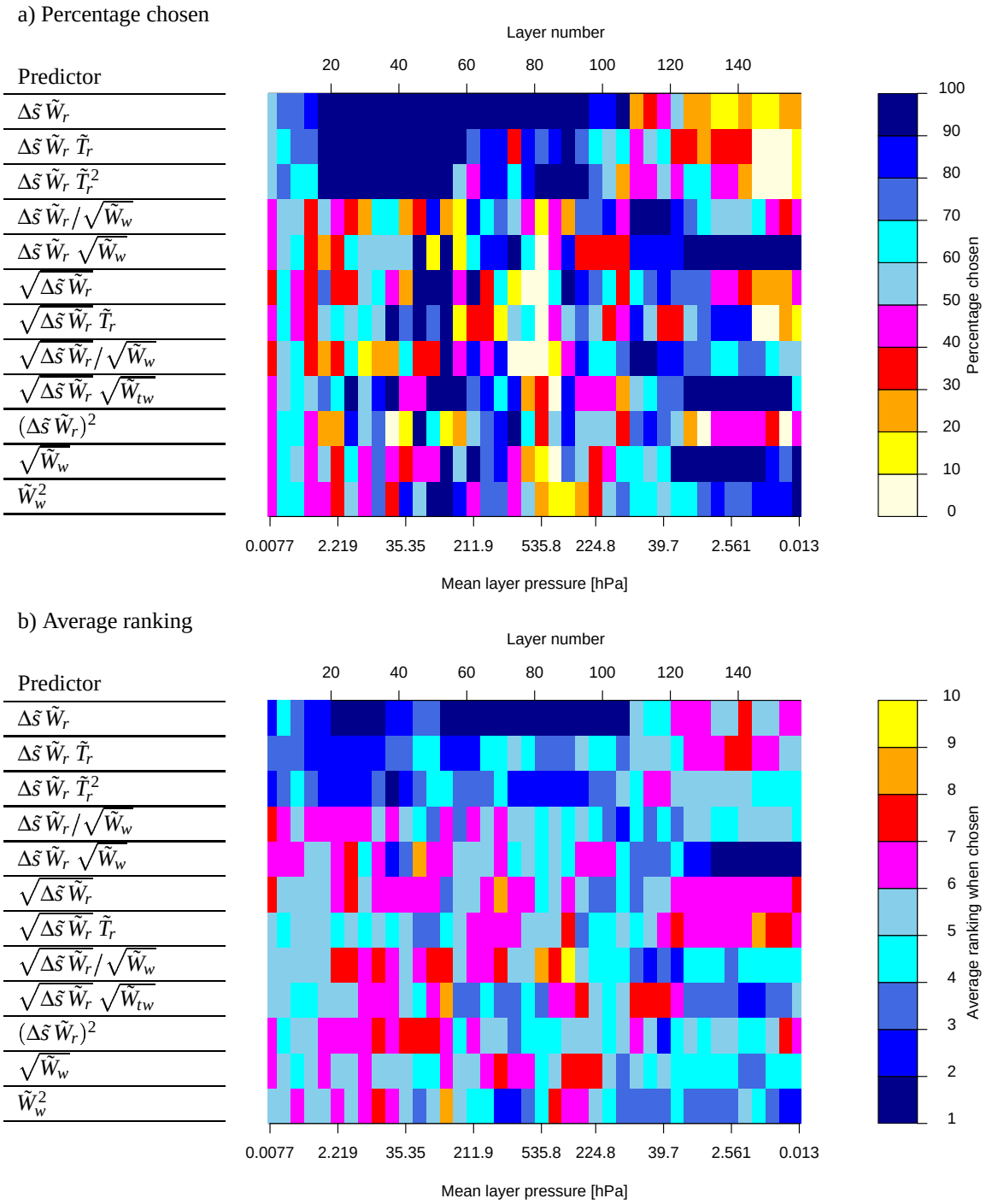

Figure 6: As Fig. 5, but for the predictors of the water vapour line absorption model, with the stepwise selection performed over the C-band.

a) Percentage chosen

Predictor
$\Delta\tilde{s}\,\tilde{O}_r$
$\Delta\tilde{s}\,\tilde{O}_r\,\tilde{T}_r$
$\Delta\tilde{s}\,\tilde{O}_r\,\tilde{T}_r^2$
$\Delta\tilde{s}\,\tilde{O}_r/\sqrt{\tilde{O}_w}$
$\Delta\tilde{s}\,\tilde{O}_r\,\sqrt{\tilde{O}_w}$
$\sqrt{\Delta\tilde{s}\,\tilde{O}_r}$
$\sqrt{\Delta\tilde{s}\,\tilde{O}_r\,\tilde{T}_r}$
$(\Delta\tilde{s}\,\tilde{O}_r)^{1.5}/\sqrt{\tilde{O}_w}$
$\sqrt{\tilde{O}_{tw}}$
$\tilde{O}_{tw}^2$
$\sqrt{\tilde{O}_w}$
$\tilde{O}_w^2$
$\Delta\tilde{s}\,\tilde{T}_r^3$

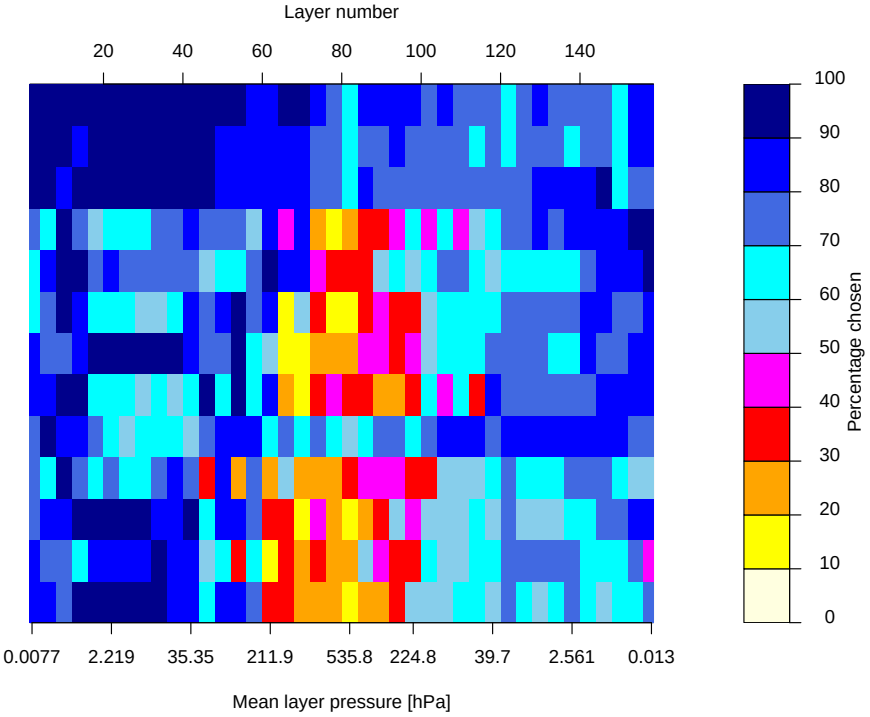

b) Average ranking

Predictor
$\Delta\tilde{s}\,\tilde{O}_r$
$\Delta\tilde{s}\,\tilde{O}_r\,\tilde{T}_r$
$\Delta\tilde{s}\,\tilde{O}_r\,\tilde{T}_r^2$
$\Delta\tilde{s}\,\tilde{O}_r/\sqrt{\tilde{O}_w}$
$\Delta\tilde{s}\,\tilde{O}_r\,\sqrt{\tilde{O}_w}$
$\sqrt{\Delta\tilde{s}\,\tilde{O}_r}$
$\sqrt{\Delta\tilde{s}\,\tilde{O}_r\,\tilde{T}_r}$
$(\Delta\tilde{s}\,\tilde{O}_r)^{1.5}/\sqrt{\tilde{O}_w}$
$\sqrt{\tilde{O}_{tw}}$
$\tilde{O}_{tw}^2$
$\sqrt{\tilde{O}_w}$
$\tilde{O}_w^2$
$\Delta\tilde{s}\,\tilde{T}_r^3$

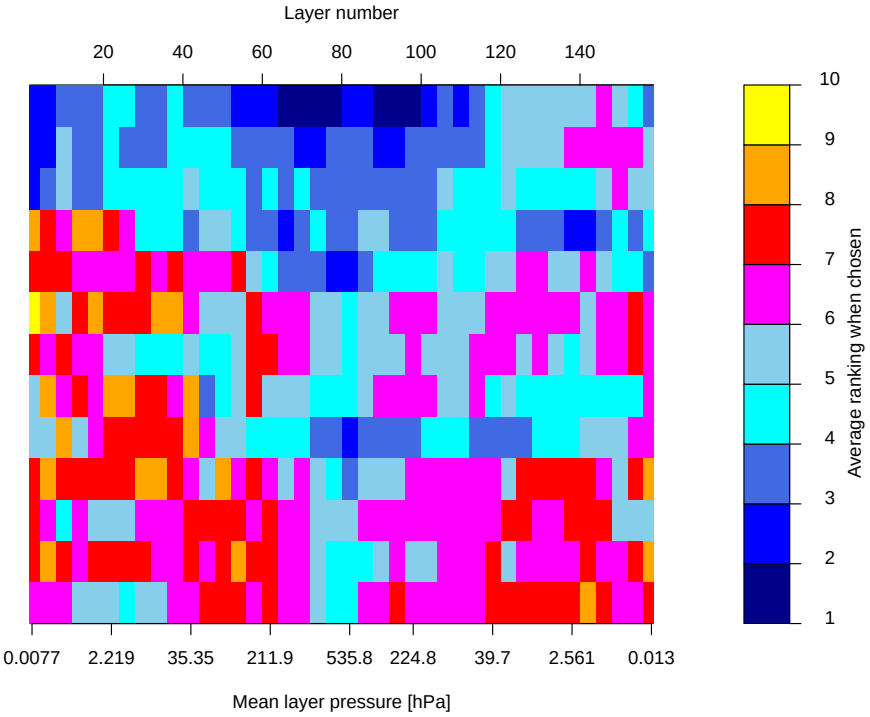

Figure 7: As Fig. 5, but for the predictors of the ozone model, with the stepwise selection performed over the AB-band.

3 Validation of the fast model

In this section we study the accuracy of RTMIPAS by comparing pencil beam radiances and transmittances from RTMIPAS with RFM equivalents for the dependent profile set and for a set of profiles independent of the regression coefficients. Note that we validate RTMIPAS against results from the same LBL model used in the training phase, thus characterising the "fast model errors" only. Spectroscopic errors in the LBL model are not addressed here.

It is worth noting here that we present results for all spectral points for which RTMIPAS has been developed, whether or not these will be used in the future assimilation of MIPAS data in the ECMWF system. Given the large number of channels of MIPAS, it is necessary to select a subset of channels for any quantitative analyses, as for instance done in the ESA retrievals (e.g., Ridolfi et al. 2000). This selection will give the opportunity to exclude channels with contributions from unmodeled gases or with too large fast model errors, using methods described by Dudhia et al. (2002a).

3.1 Radiance errors for the dependent profile set

For the dependent profile set, RTMIPAS can reproduce the RFM radiance spectra to a level of accuracy below the noise level of the MIPAS instrument for most channels and pencil beams over the range considered by RTMIPAS. Figures 8 to 12 show the standard deviation and the mean of the RTMIPAS-RFM radiance differences, normalised by the apodised instrument noise (i.e., error-to-noise ratio). For the noise specification, in-flight values of the well-studied orbit 2081 have been used (Fig. 1). For display purposes, we show the maximum and the mean error-to-noise ratio for each 40-channel interval (1 cm^{-1}) for each pencil beam. Note that displaying the maximum in each 40-channel interval emphasises the poorest performance of RTMIPAS (as just one poorly modelled channel may represent the whole spectral interval), whereas the mean may be reduced due to a good performance for channels with little variability and therefore little use in data assimilation. The Figures exhibit a very good performance of RTMIPAS. More than 92% of the channels typically show standard deviations of less than half the instrument noise for each pencil beam (Figures 13, 15, 17, 19, 21), with an even better performance for the higher pencil beams. Radiance biases are also usually small (typically less than $\frac{1}{10}$th of the instrument noise), except for the lowest pencil beams (e.g., Figures 10 to 12, 14, 16, 18, 20, 22).

As expected, the performance of RTMIPAS differs with spectral band. Overall, the MIPAS B- and C-band with strong water vapour absorption show the smallest error-to-noise ratio (e.g., Figures 17 to 20). This is largely due to the small variability of water vapour in the stratosphere. The AB-band with predominantly ozone absorption shows the poorest statistics (e.g., Fig. 15), particularly in the regions of strong ozone absorption around 1020-1075 cm^{-1}, or in the 1070-1170 cm^{-1} region at lower tangent heights. Further investigations reveal that these errors are predominantly introduced by the ozone transmittance model. Similarly, the fast model errors and biases in the 750-800 cm^{-1} wavenumber region of the A-band are also mainly introduced by the ozone transmittance model. Biases tend to be most pronounced at lower levels in the A- and AB-band (e.g., Figures 14 and 16), whereas the other bands exhibit negligible biases throughout (Figures 10 to 12). The biases at lower levels are not considered problematic, as the respective channels could be avoided in the assimilation, and the lowest pencil beams will frequently not be used due to cloud contamination in the observations.

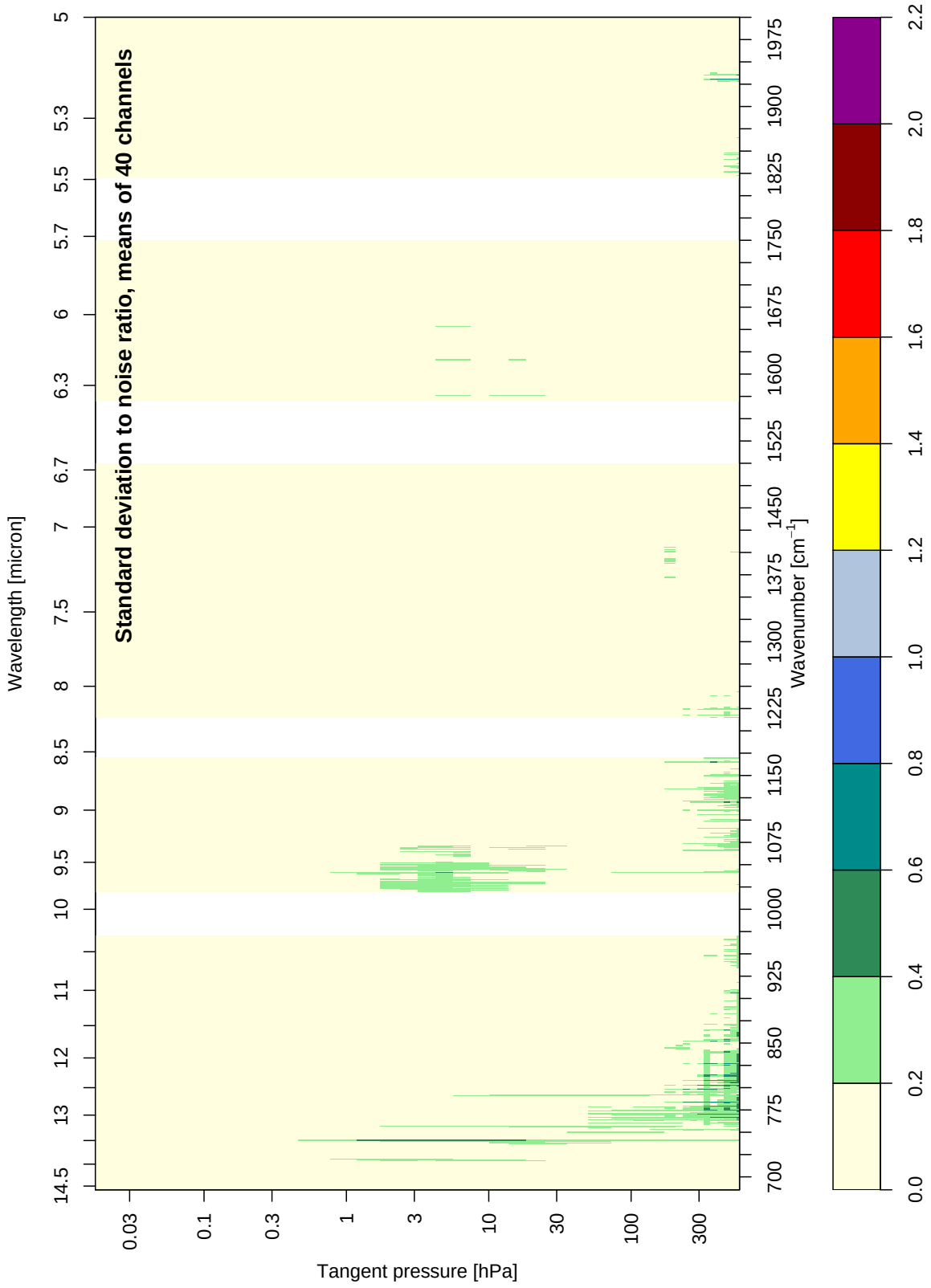

Figure 8: Standard deviation of the RTMIPAS-RFM radiance differences, scaled by the MIPAS noise, for the dependent profile set. The plot shows the mean standard deviation to noise ratio over 40 channel intervals (i.e., 1 cm^{-1} intervals) as a function of wavenumber and pencil beam pressure.

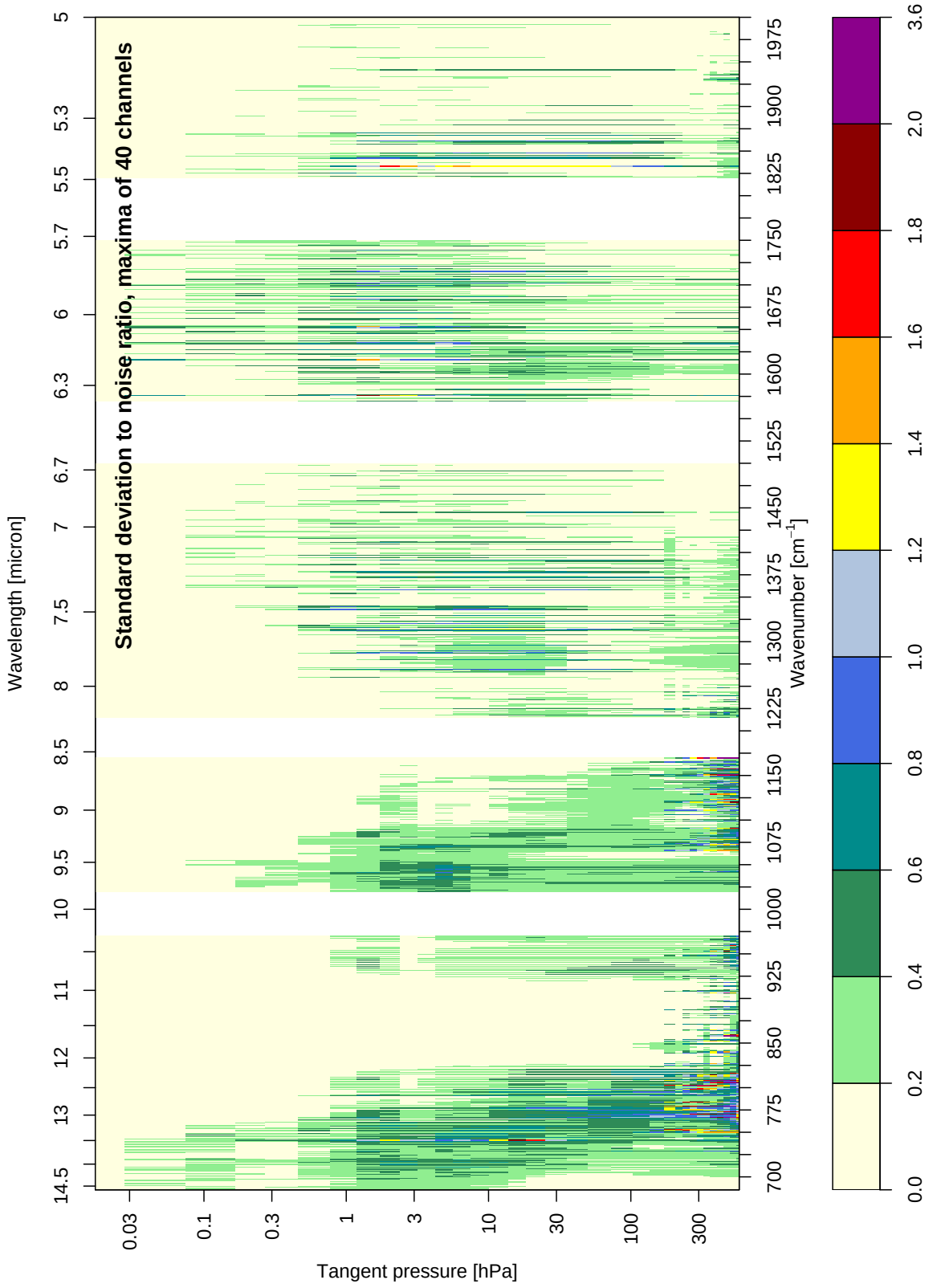

Figure 9: Standard deviation of the RTMIPAS-RFM radiance differences, scaled by the MIPAS noise, for the dependent profile set. The plot shows the maximum standard deviation to noise ratio of 40 channel intervals (i.e., 1 cm^{-1} intervals) as a function of wavenumber and pencil beam pressure.

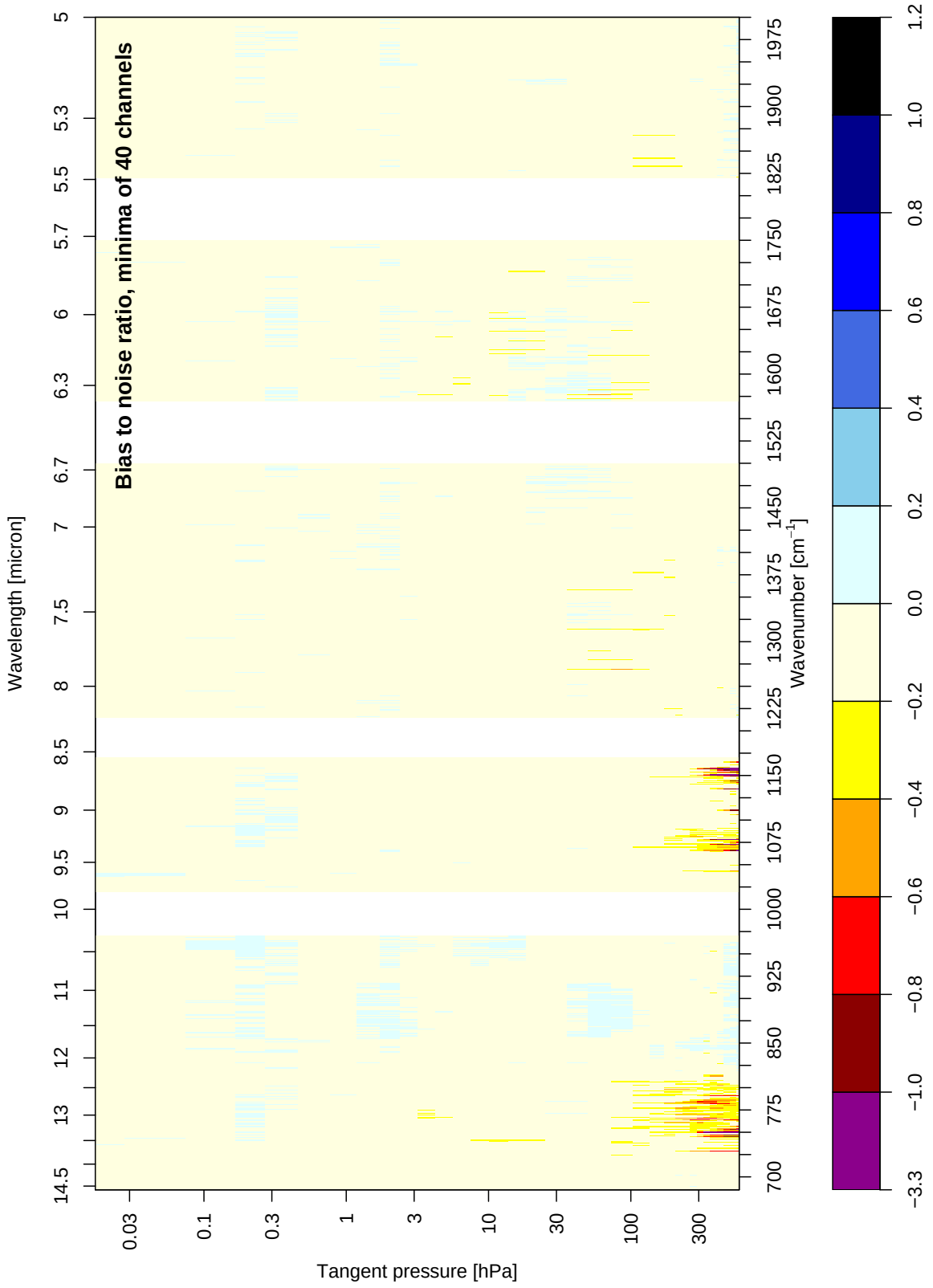

Figure 10: Mean RTMIPAS-RFM radiance differences (bias), scaled by the MIPAS noise, for the dependent profile set. The plot shows the minimum of the bias to noise ratio of 40 channel intervals (i.e., 1 cm^{-1} intervals) as a function of wavenumber and pencil beam pressure.

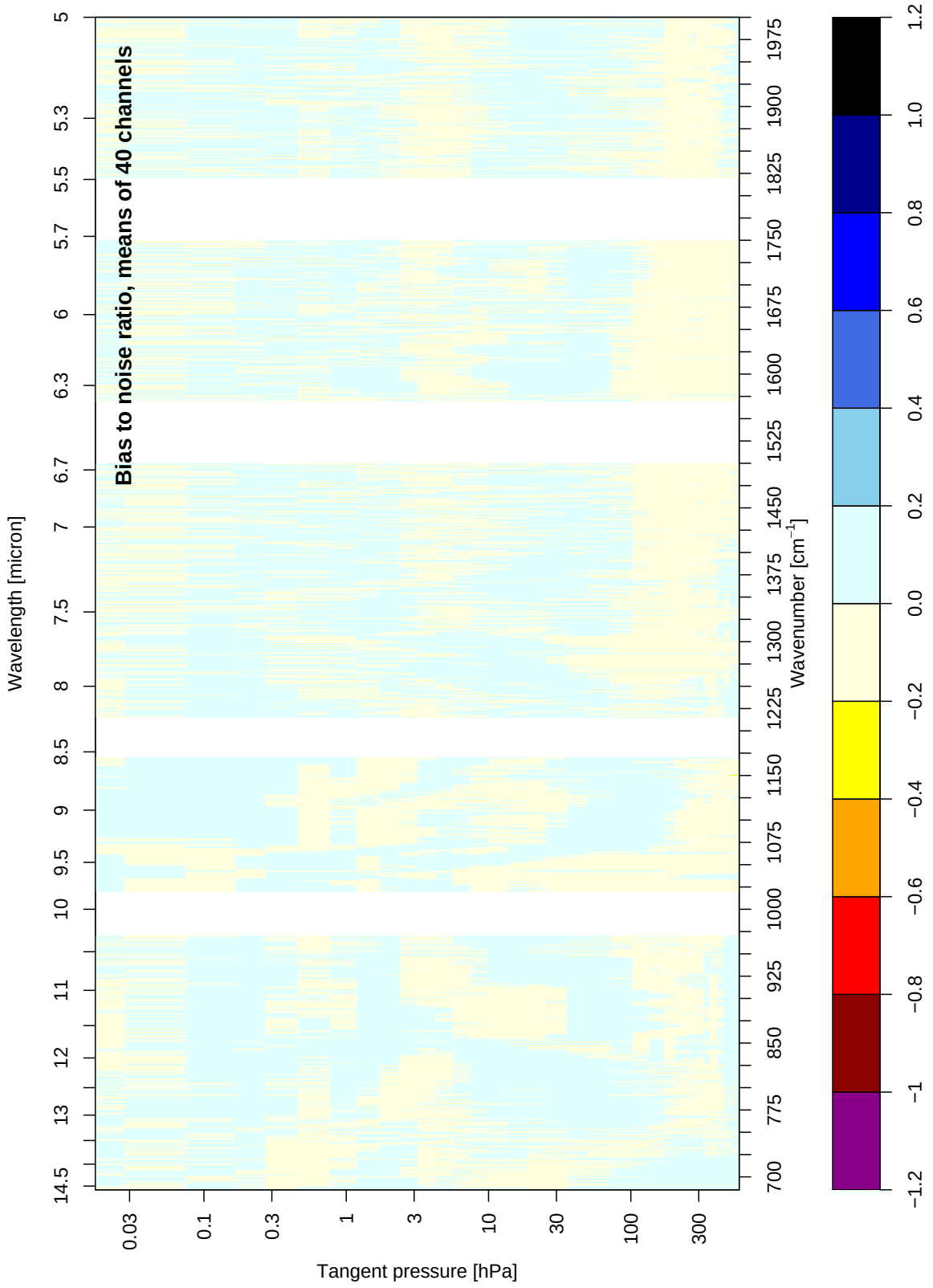

Figure 11: Mean RTMIPAS-RFM radiance differences (bias), scaled by the MIPAS noise, for the dependent profile set. The plot shows the mean of the bias to noise ratio over 40 channel intervals (i.e., 1 cm^{-1} intervals) as a function of wavenumber and pencil beam pressure.

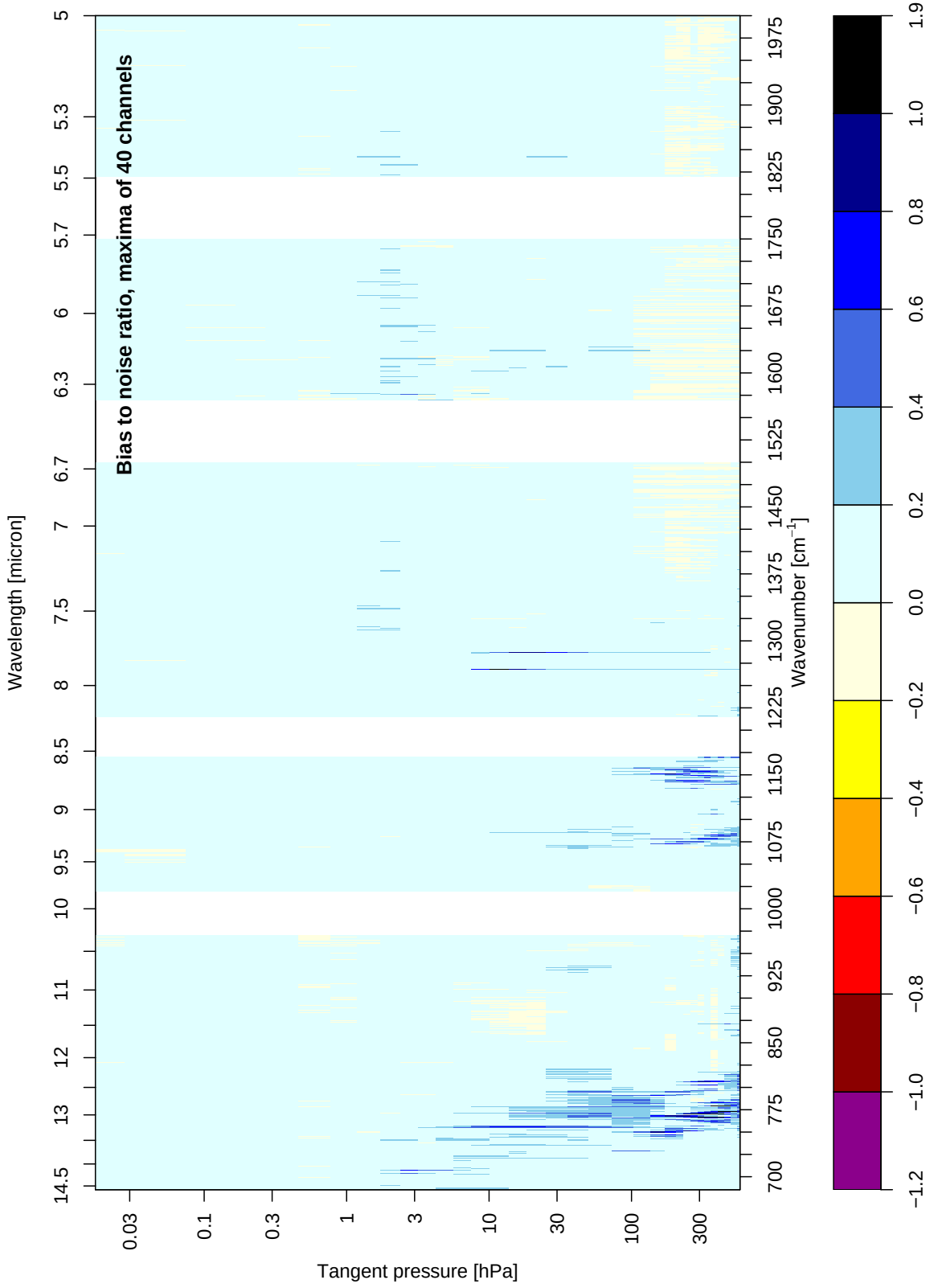

Figure 12: Mean RTMIPAS-RFM radiance differences (bias), scaled by the MIPAS noise, for the dependent profile set. The plot shows the maximum of the bias to noise ratio of 40 channel intervals (i.e., 1 cm^{-1} intervals) as a function of wavenumber and pencil beam pressure.

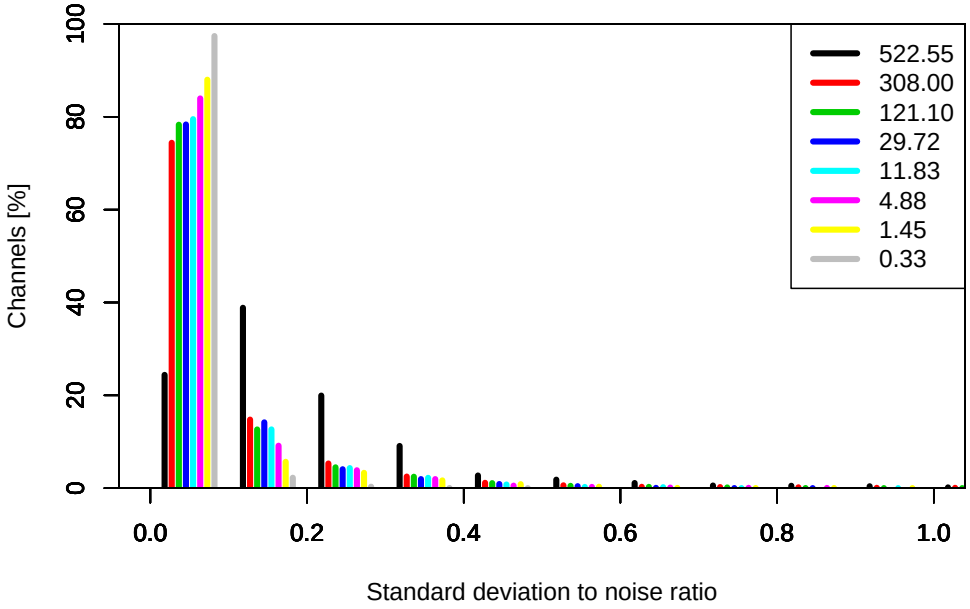

Figure 13: Distribution of the number of channels [%] in the MIPAS A-band versus the standard deviation of the RTMIPAS-RFM radiance differences, scaled by the MIPAS noise. The statistic is based on the dependent profile set. Results for 8 selected pencil beams are shown, with their tangent pressures [hPa] indicated in the legend. The binning interval is 0.1.

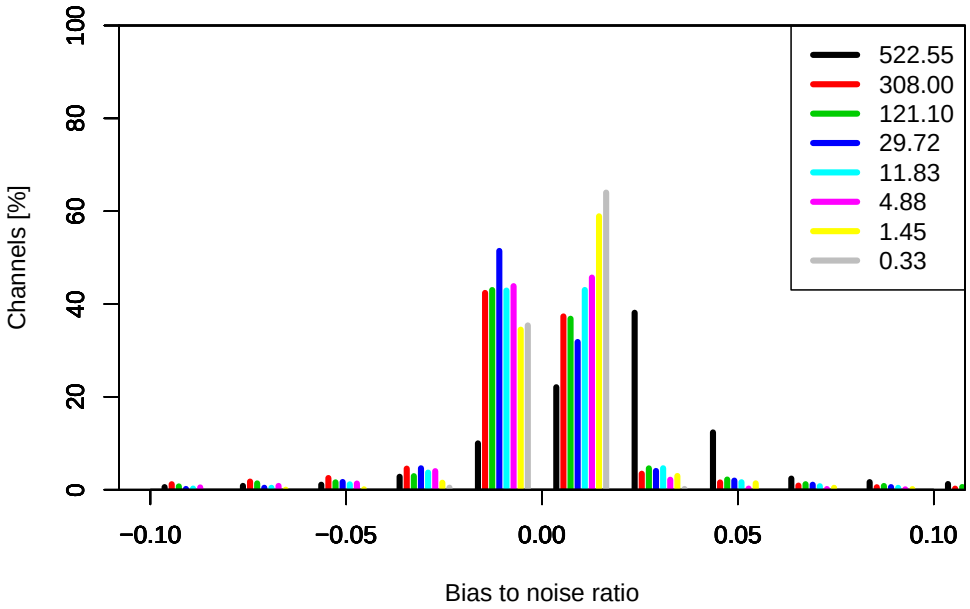

Figure 14: Distribution of the number of channels [%] in the MIPAS A-band versus the mean RTMIPAS-RFM radiance difference, scaled by the MIPAS noise. The statistic is based on the dependent profile set. Results for 8 selected pencil beams are shown, with their tangent pressures [hPa] indicated in the legend. The binning interval is 0.02.

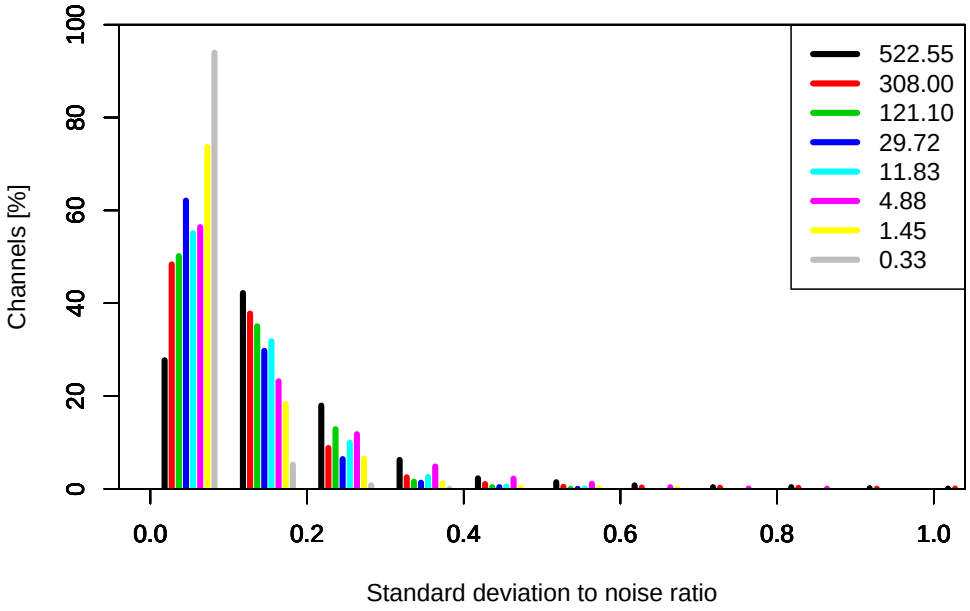

Figure 15: As Fig. 13, but for the MIPAS AB-band.

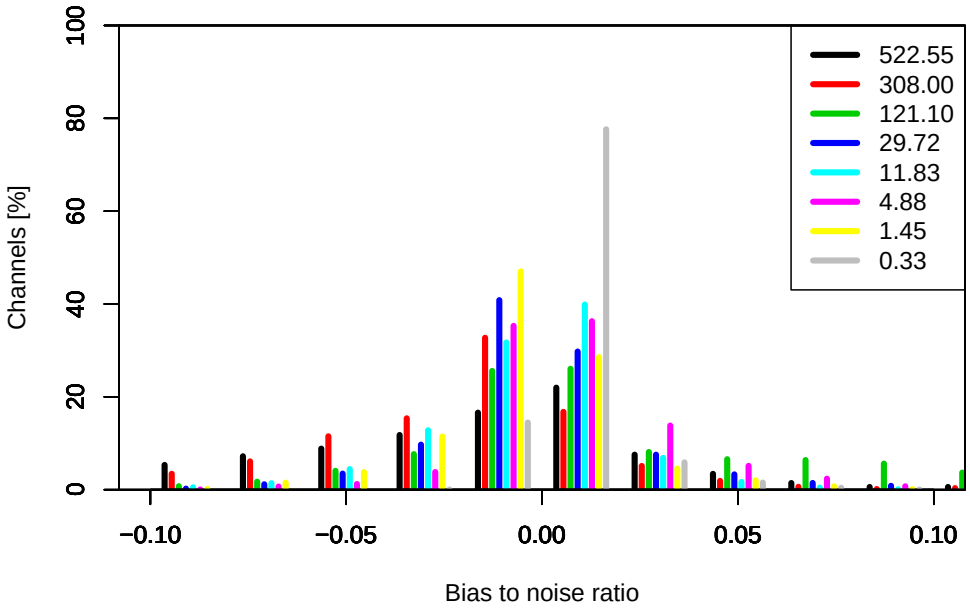

Figure 16: As Fig. 14, but for the MIPAS AB-band.

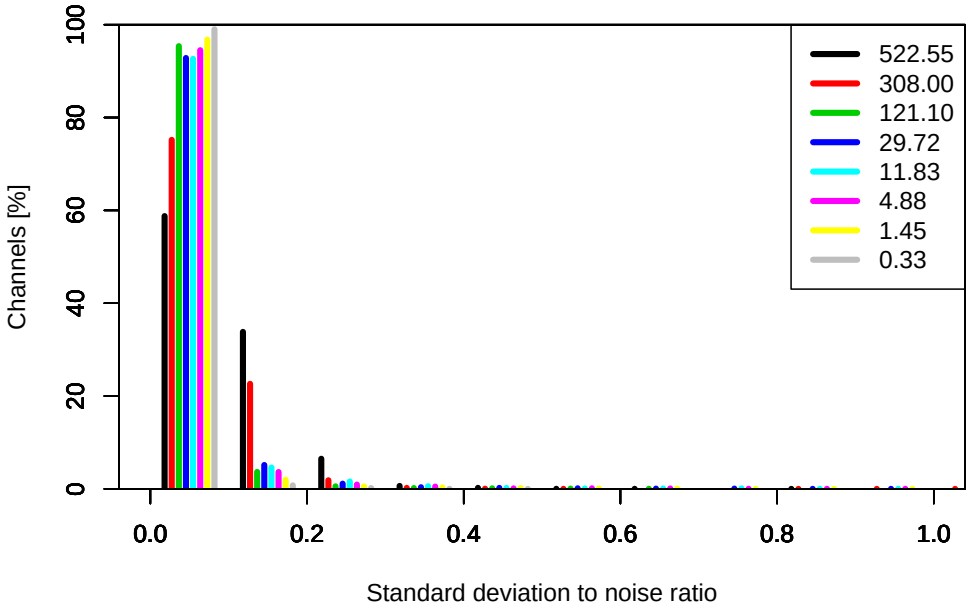

Figure 17: As Fig. 13, but for the MIPAS B-band.

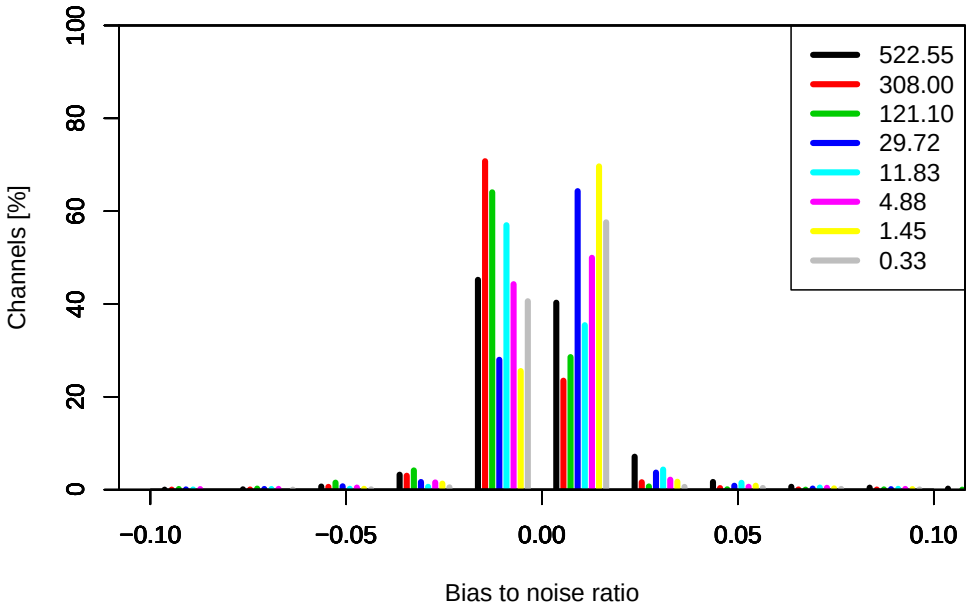

Figure 18: As Fig. 14, but for the MIPAS B-band.

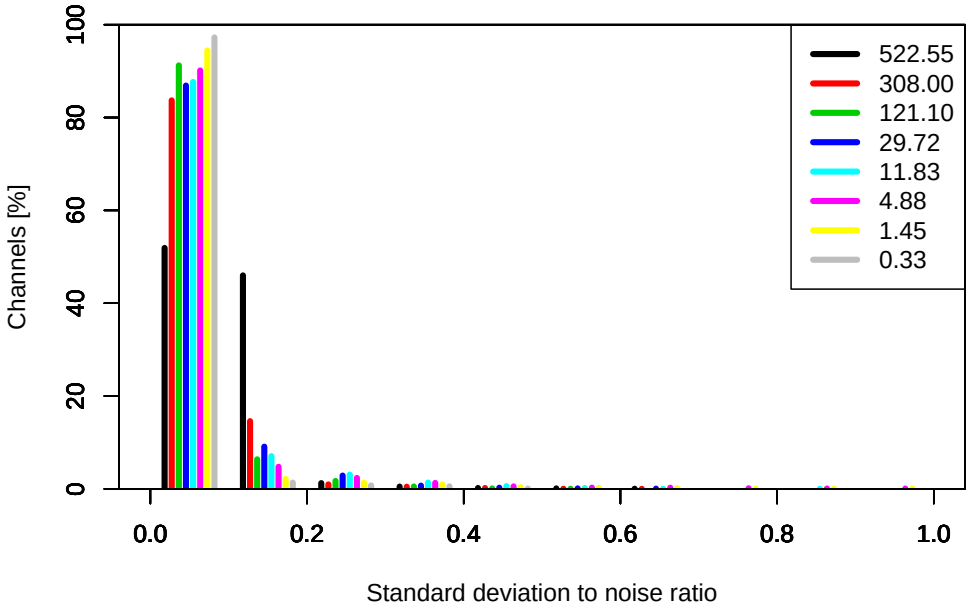

Figure 19: As Fig. 13, but for the MIPAS C-band.

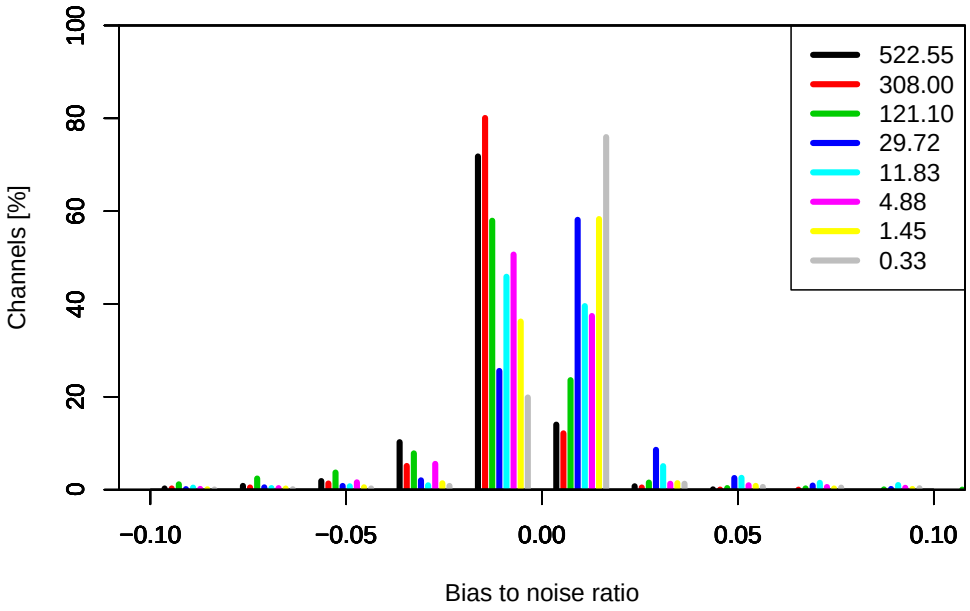

Figure 20: As Fig. 14, but for the MIPAS C-band.

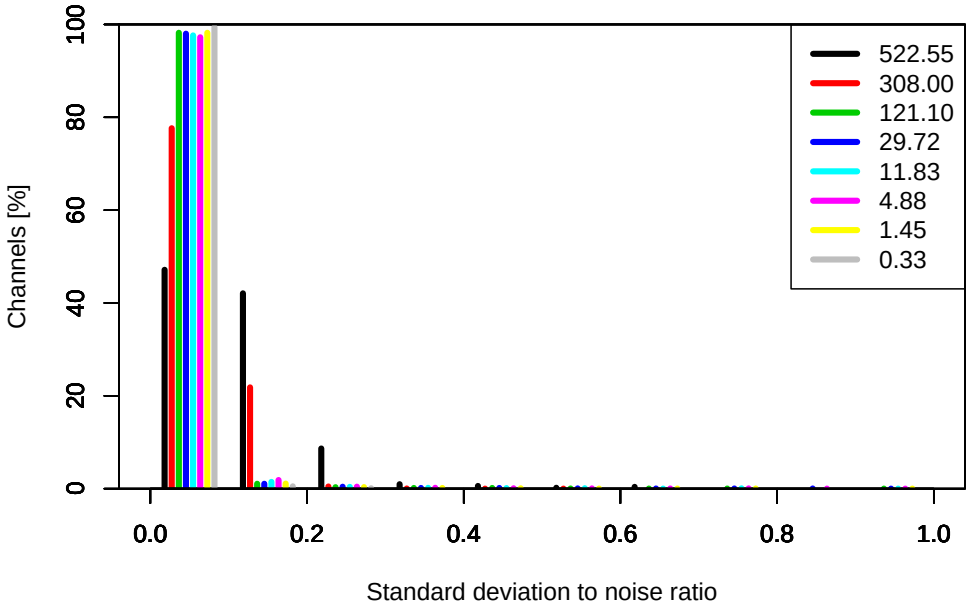

Figure 21: As Fig. 13, but for the MIPAS D-band up to 2000 cm^{-1}.

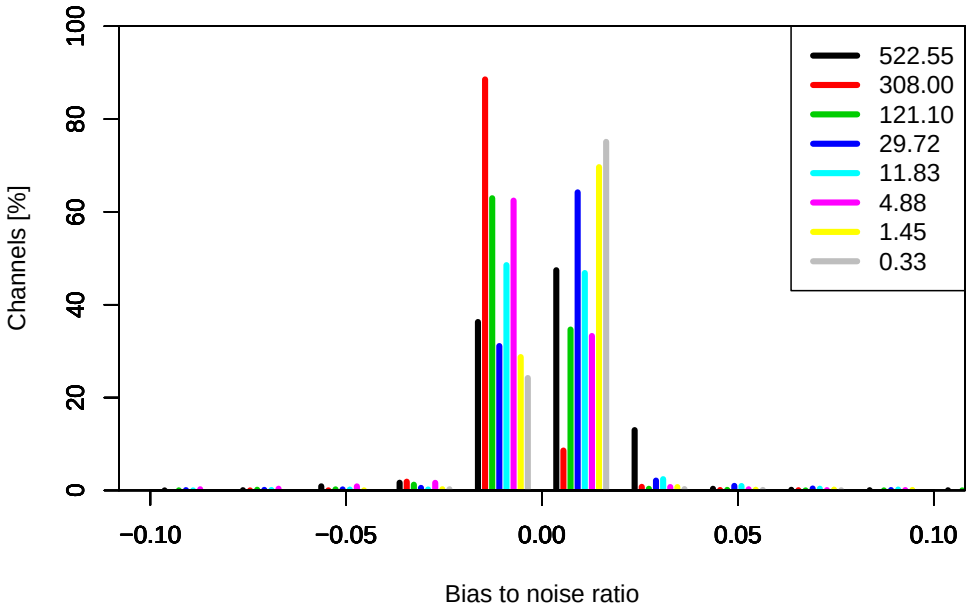

Figure 22: As Fig. 14, but for the MIPAS D-band up to 2000 cm^{-1}.

3.2 Transmittance errors for the dependent profile set

While the evaluation in terms of radiances is most relevant for the application of RTMIPAS, a characterisation of the model performance in terms of transmittances can give further insights and may point to areas where improvements are possible.

Overall, root mean squared (RMS) differences between RTMIPAS and the RFM transmittances are typically around $10^{-4} - 10^{-5}$, and the maximum RMS difference rarely exceeds 0.005 (Figures 23, 25, 27, 29, 31). The errors are comparable to those found in Matricardi (2003) for RTIASI, indicating that the quality of the fast transmittance model in RTMIPAS is comparable to the one for similar regression-based models for the nadir viewing geometry. The lowest pencil beams in the C- and D-band (with considerable water vapour absorption) show the poorest performance in terms of transmittance RMS differences (Figures 29 and 31). This is most likely due to the larger water vapour variability for the tropospheric channels.

The region where the maximum transmittance error occurs tends to depend on the tangent pressure of the pencil beams (Figures 24, 26, 28, 30, 32). For the lowest pencil beams it occurs more often on the satellite-ward side of the tangent point, whereas for the pencil beams with tangent points in the stratosphere the maximum RMS difference tends to occur on the space-ward side of the tangent point. The former reflects the fact that many of the lower limb rays become opaque ($\tau \rightarrow 0.0$) at or around the tangent layer, whereas the latter may be due to the difficulty of fitting the larger variability of satellite-ward path conditions on the space-ward side of the tangent point. This larger variability is a result of the fact that for a given level on the space-ward side of the tangent point, the level-to-satellite path can cross through a different number of layers below the level considered, depending on the height of the tangent point.

The accuracy of the modelled transmittances is, to some extent, affected by the large variability of the path lengths encountered in layers which are used as tangent layers. Frequently, the largest transmittance errors occur at a level which is used as a tangent level for another pencil beam on the satellite-ward side, and at the level just above on the space-ward side of the tangent point. This is associated with the larger variability in the layer path lengths for these layers, with the longest path lengths occurring when the layer is used as a tangent layer. For layers used as tangent layers, the ratio between the longest and the shortest layer path length which can be encountered is typically more than twice as large as for neighbouring layers, with this ratio exceeding 10 for some middle layers. In comparison, in fast models for nadir viewing a factor of 2.25 is typically encountered. One option to improve the transmittance model of RTMIPAS would be to use two regression models: one to apply when the respective layer is a tangent layer, and one for all other situations. Given the good performance of RTMIPAS in terms of radiances in the current configuration we have not pursued this option further.

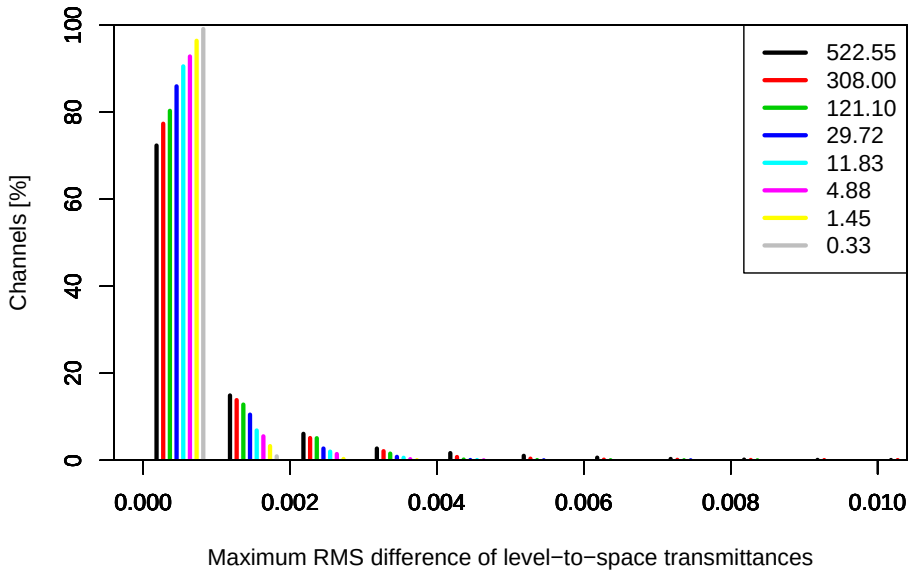

Figure 23: Distribution of the number of channels [%] in the MIPAS A-band versus the channel maximum RMS of the RTMIPAS-RFM differences in the level-to-satellite transmittances. The statistic is based on the dependent profile set. Results for 8 selected pencil beams are shown, with their tangent pressures [hPa] indicated in the legend. The binning interval is 0.001.

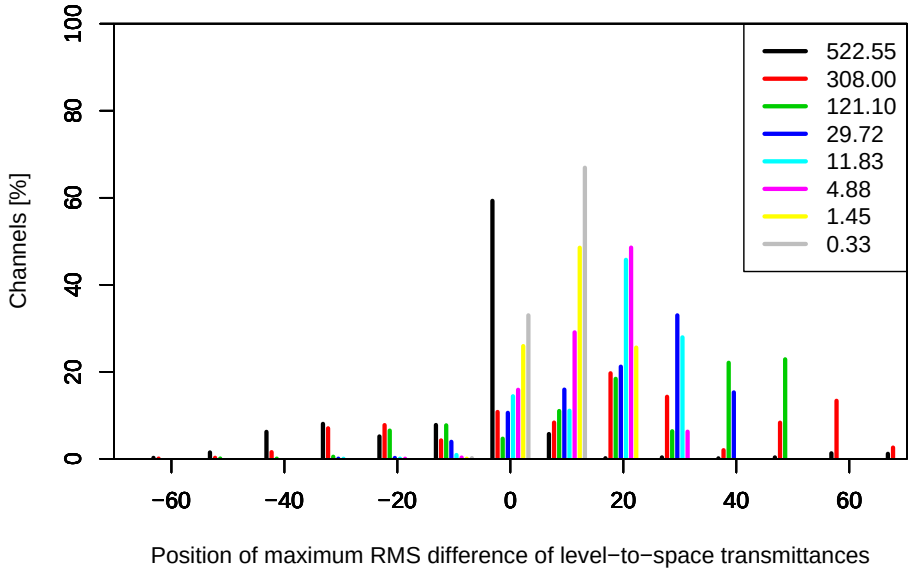

Figure 24: Distribution of the number of channels [%] in the MIPAS A-band versus the level at which the channel maximum RMS of the RTMIPAS-RFM differences in the level-to-satellite transmittances shown in Fig. 23 is found. The level is calculated relative to the tangent point (located at 0), with negative level numbers for the satellite-ward side of the ray, and positive level numbers for the other side. The statistic is based on the dependent profile set. Results for 8 selected pencil beams are shown, with their tangent pressures [hPa] indicated in the legend. The binning interval is 10 levels.

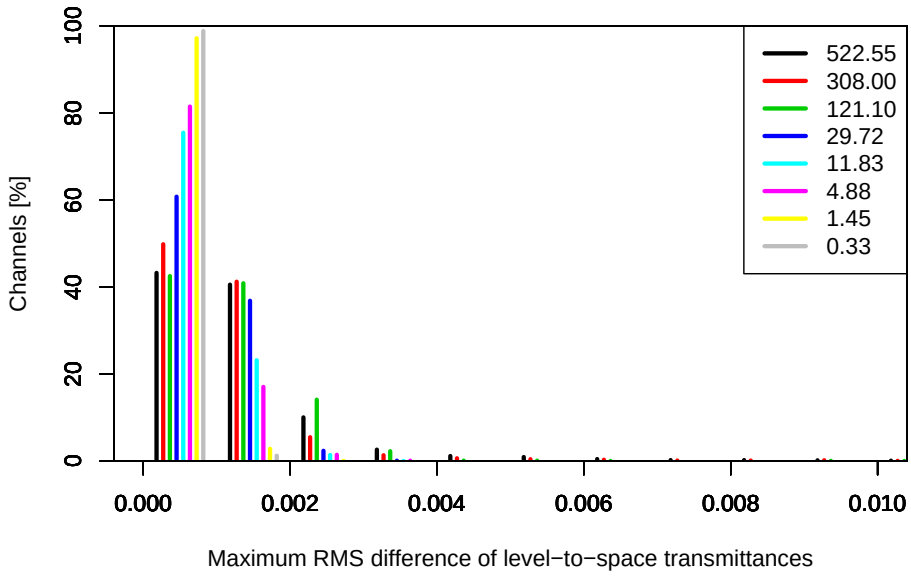

Figure 25: As Fig. 23, but for the MIPAS AB-band.

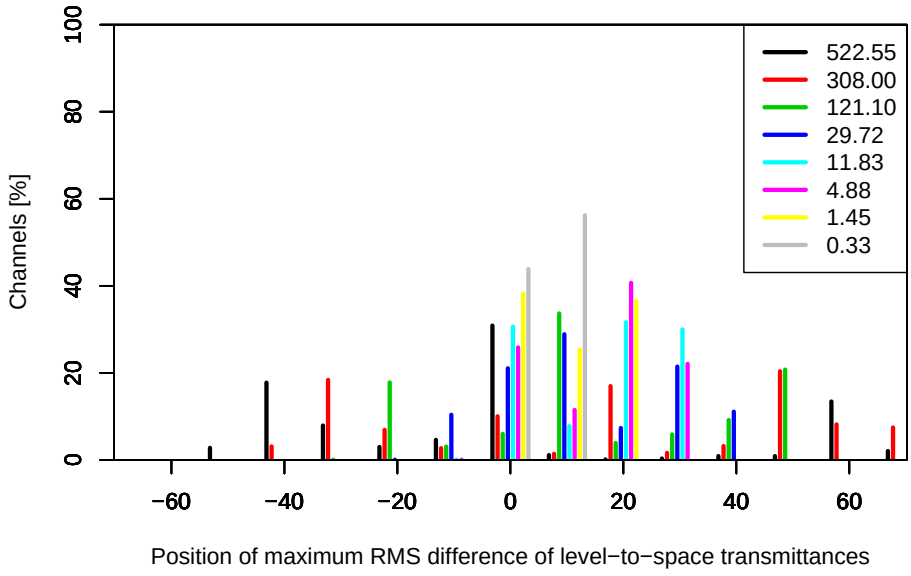

Figure 26: As Fig. 24, but for the MIPAS AB-band.

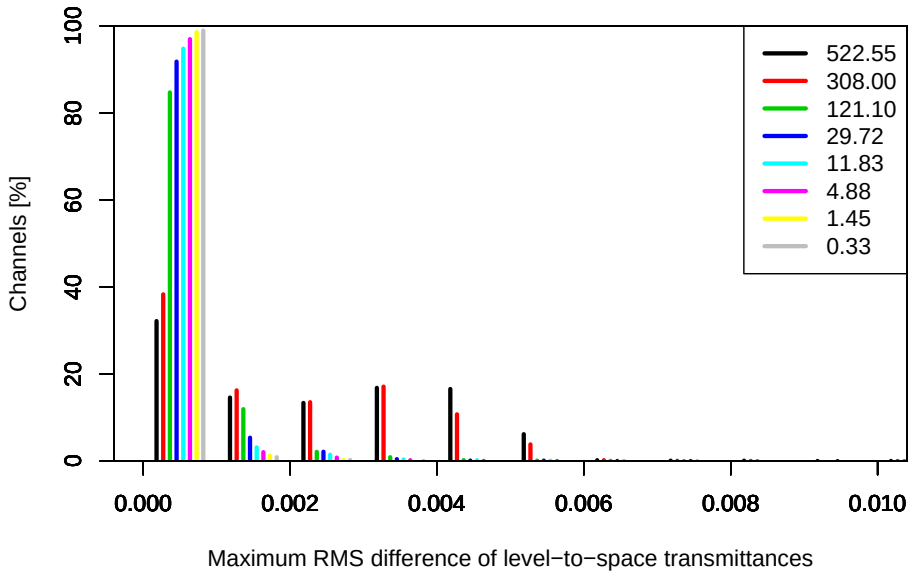

Figure 27: As Fig. 23, but for the MIPAS B-band.

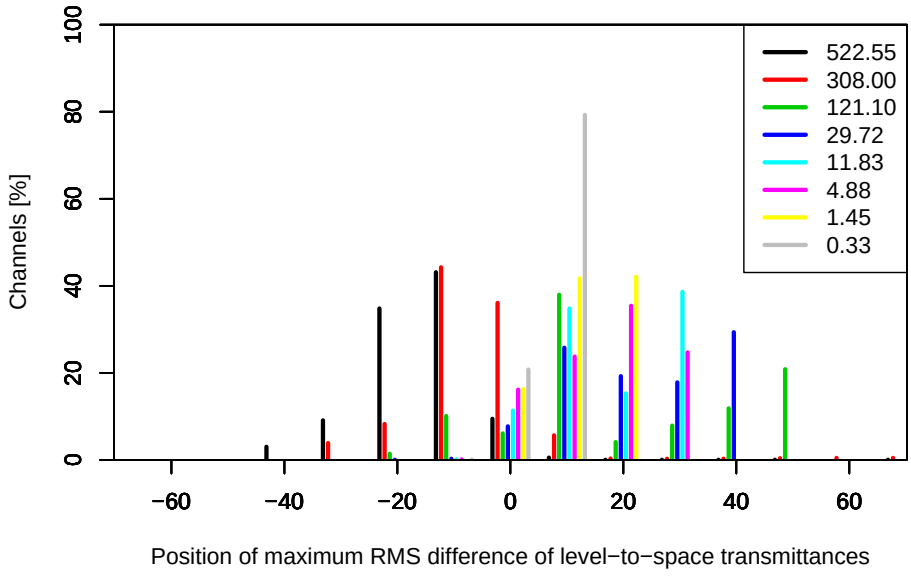

Figure 28: As Fig. 24, but for the MIPAS B-band.

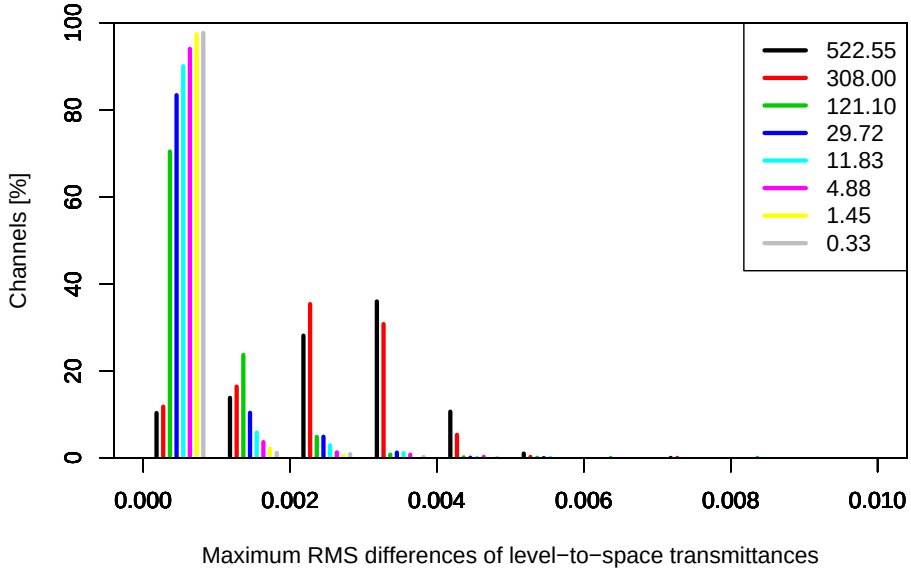

Figure 29: As Fig. 23, but for the MIPAS C-band.

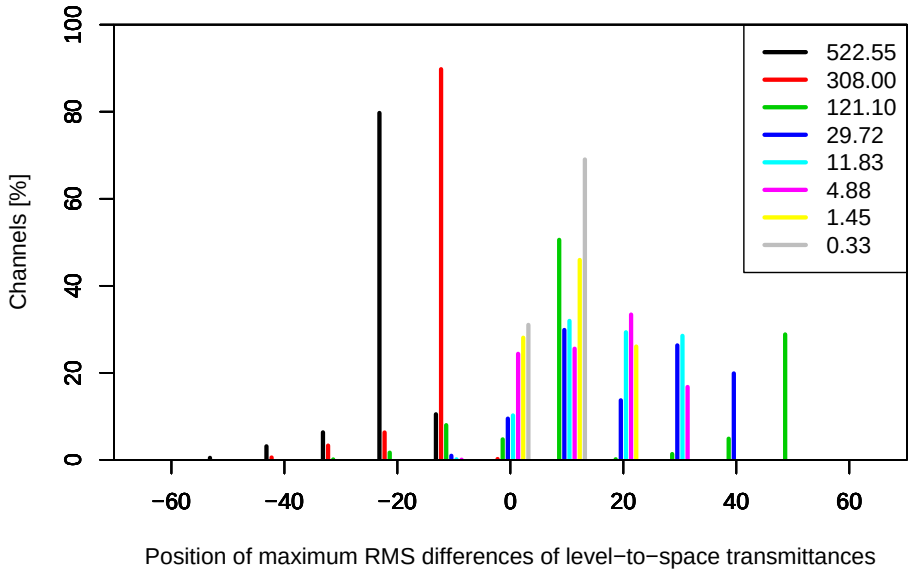

Figure 30: As Fig. 24, but for the MIPAS C-band.

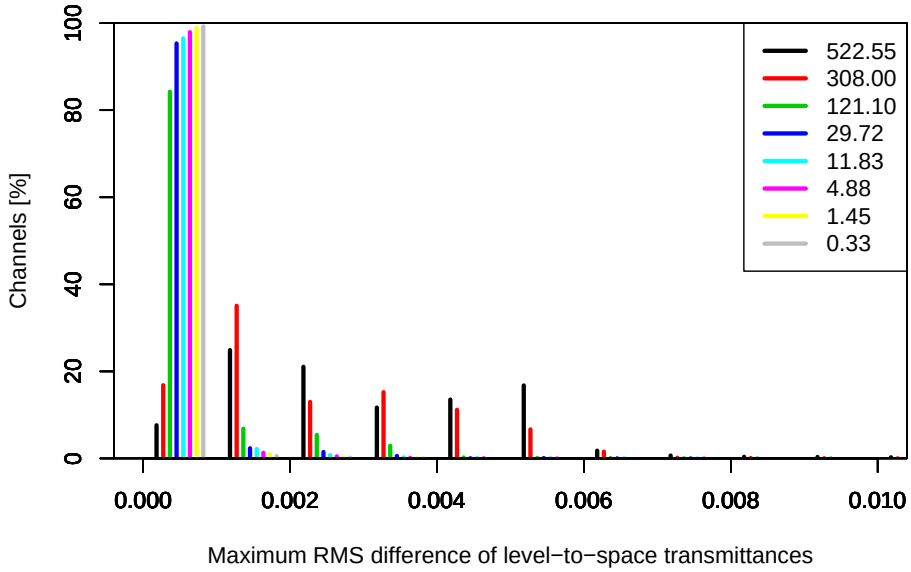

Figure 31: As Fig. 23, but for the MIPAS D-band below 2000 cm^{-1}.

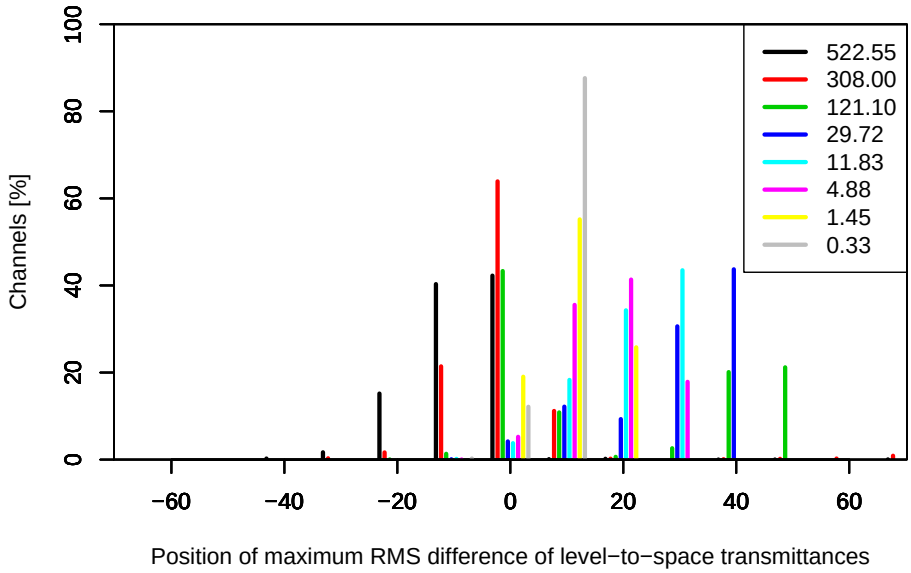

Figure 32: As Fig. 24, but for the MIPAS D-band below 2000 cm^{-1}.

3.3 Water vapour continuum transmittance errors for the dependent profile set

RTMIPAS uses a separate regression model for the water vapour continuum, trained on a separate database of transmittances from the CKD 2.4 water vapour continuum model (Clough et al. 1989). The database is based on the same 46 diverse profiles shown in Fig. 4.

The transmittance errors introduced by the fast model for the water vapour continuum alone are fairly small, and the maximum RMS differences of the RTMIPAS-RFM transmittances exceeds 0.001 only for the lowest pencil beams with tangent pressures well in the troposphere (Fig. 33). The error pattern and the magnitude of the error are in good agreement with results obtained by Matricardi (2003), showing that the regression model can be successfully adapted from the nadir geometry to limb viewing.

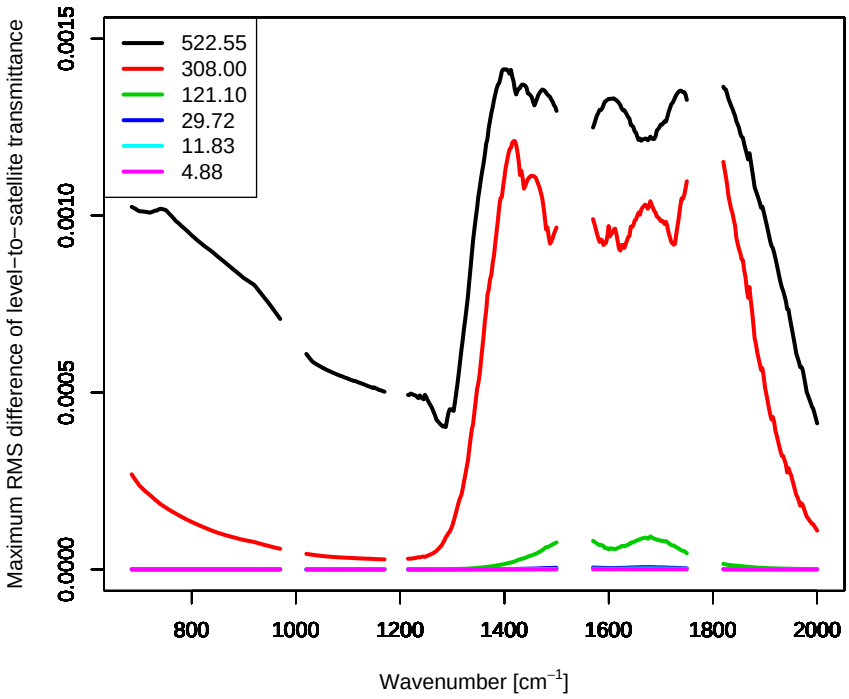

Figure 33: Channel maximum RMS of the RTMIPAS-RFM differences in the level-to-satellite transmittances for the water vapour continuum model for the dependent profile set. Results for 6 selected pencil beams are shown, with their tangent pressures [hPa] indicated in the legend.

3.4 Radiance errors for an independent profile set

We will now characterise the fast model errors for RTMIPAS for a quasi-independent set of 53 profiles. This set has been sampled from ERA-40 data in a similar way as the training set, but provides profiles from atmospheric conditions taken from different times or locations. Note that for the statistical independence of the independent profile set, the independent set should not be sampled from the same compilation of profiles as the training set, but should instead be based on a completely different source (e.g., sonde observations). However, no other profile set was available which captures the atmospheric variability and provides thermodynamically consistent temperature, water vapour, and ozone profiles at sufficient quality throughout the vertical range considered by RTMIPAS. Our choice of the independent set is not considered a major drawback since the primary aim of RTMIPAS is data assimilation within the ECMWF model.

Figures 34 to 38 show noise-normalised standard deviations and means of RTMIPAS-RFM radiance differences for all pencil beams. The Figures can be compared with Figures 8 to 12 for the dependent set.

The performance of RTMIPAS for the independent set of profiles is similar to that for the dependent set of profiles, with standard deviations of the RTMIPAS-RFM radiance differences below the noise level of the MIPAS instrument for most channels and pencil beams. The largest increases in the standard deviation or the mean of the RTMIPAS-RFM differences tend to occur for the lowest pencil beams (compare Figures 39 to 48 with Figures 13 to 22, respectively). In addition, there is a slight increase in the standard deviation of the RTMIPAS-RFM differences at about 50-100 hPa in the A- and the AB-band, and the biases for the channels with the largest biases in the A- and the AB-band are also somewhat larger. However, overall, the increase in the errors when moving to the independent profile set is smaller than what is typically encountered in similar fast models for the nadir geometry (Matricardi 2003). This is likely related to the particular testing dataset used: Matricardi (2003) uses an independent set of 117 profiles that originates from a different source as the training data with ozone profiles added from climatology and thus not necessarily thermodynamically consistent. In our case, fewer profiles are used and they are from the same source as the training set, and these profiles are thermodynamically consistent. Nevertheless, the similar performance for the independent and the dependent sets of profiles suggests that 46 profiles are adequate for the training of RTMIPAS.

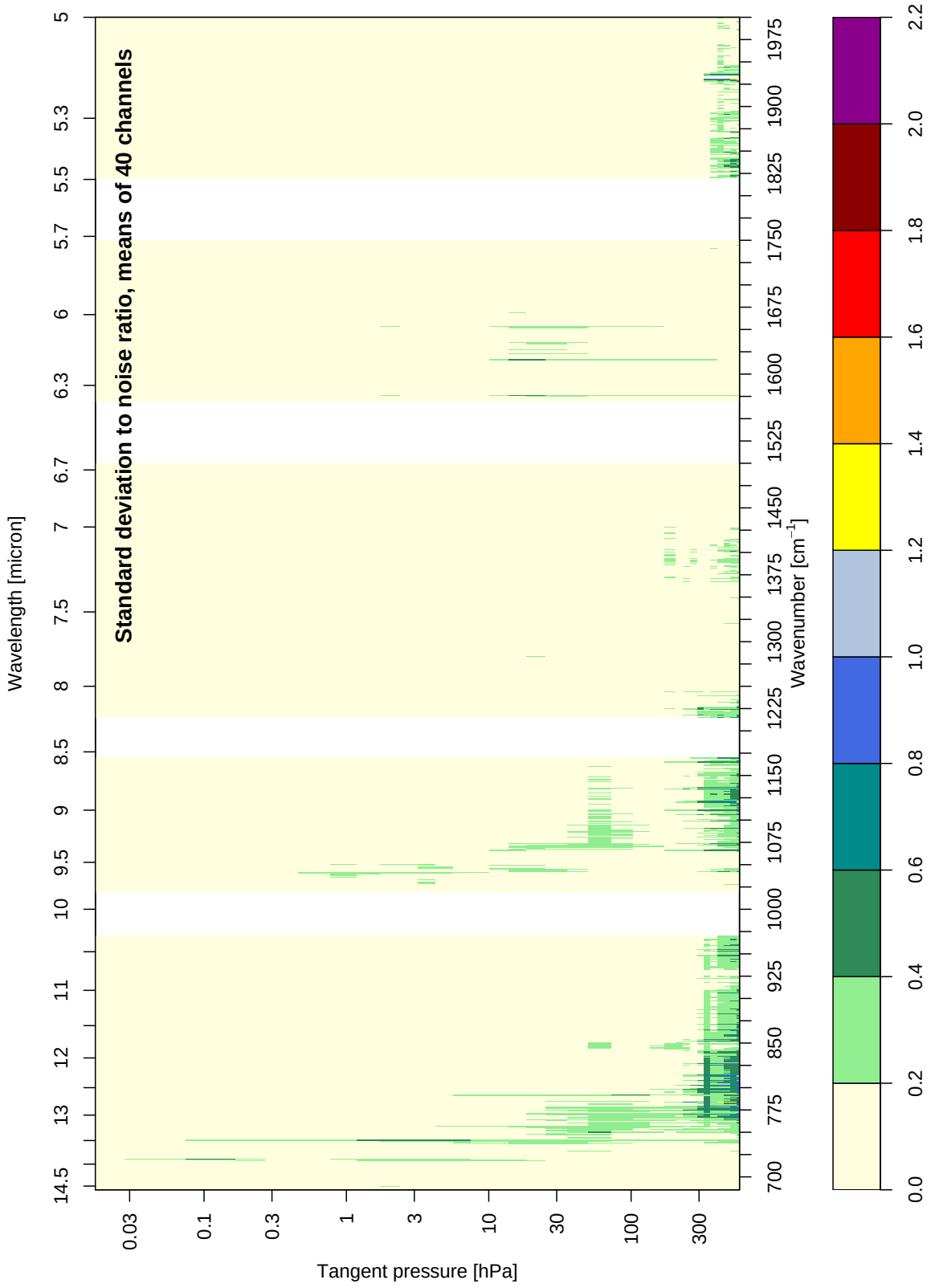

Figure 34: Standard deviation of the RTMIPAS-RFM radiance differences, scaled by the MIPAS noise, for the independent profile set. The plot shows the mean standard deviation to noise ratio over 40 channel intervals (i.e., 1 cm^{-1} intervals) as a function of wavenumber and pencil beam pressure.

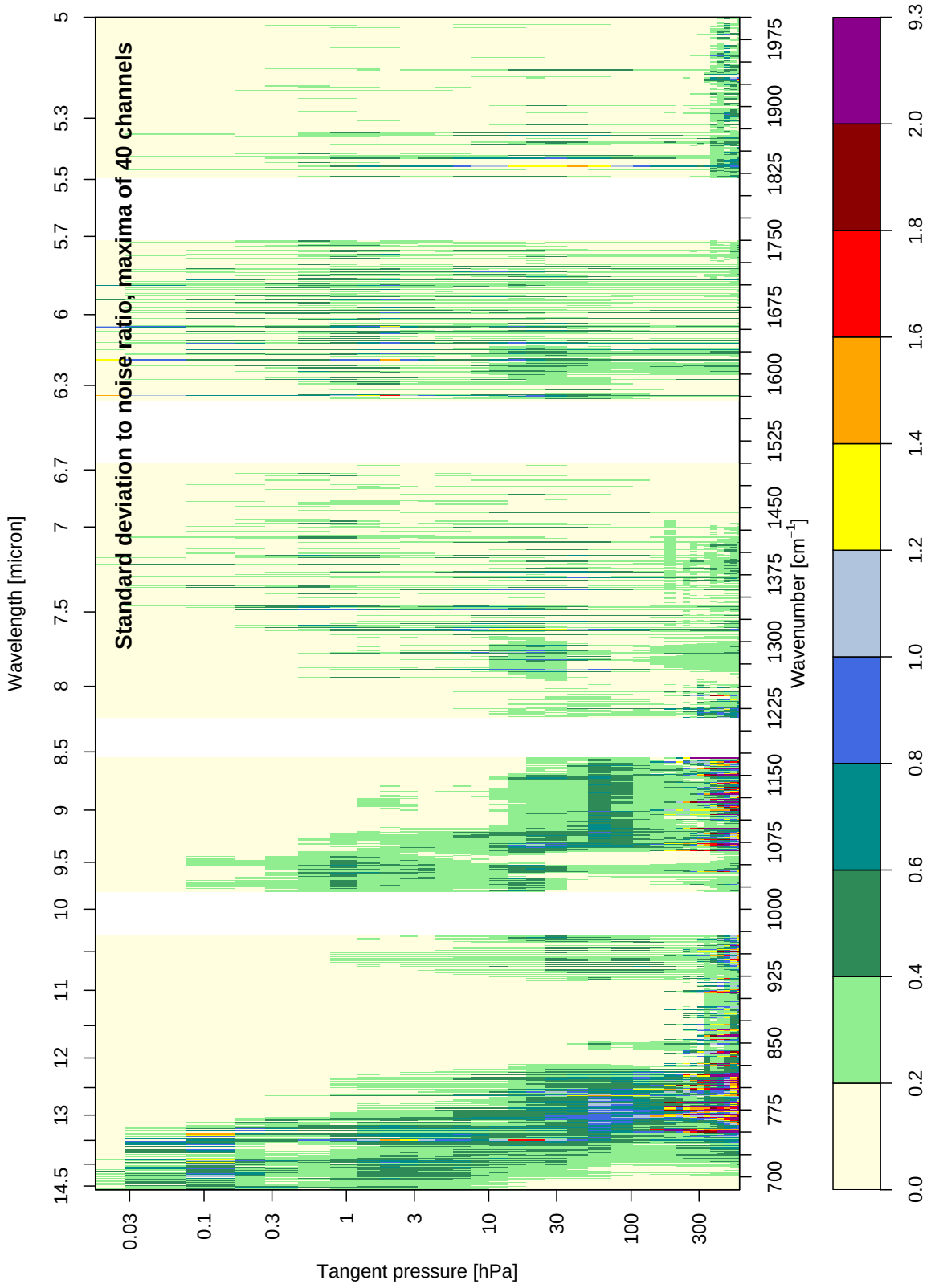

Figure 35: Standard deviation of the RTMIPAS-RFM radiance differences, scaled by the MIPAS noise, for the independent profile set. The plot shows the maximum standard deviation to noise ratio of 40 channel intervals (i.e., 1 cm^{-1} intervals) as a function of wavenumber and pencil beam pressure.

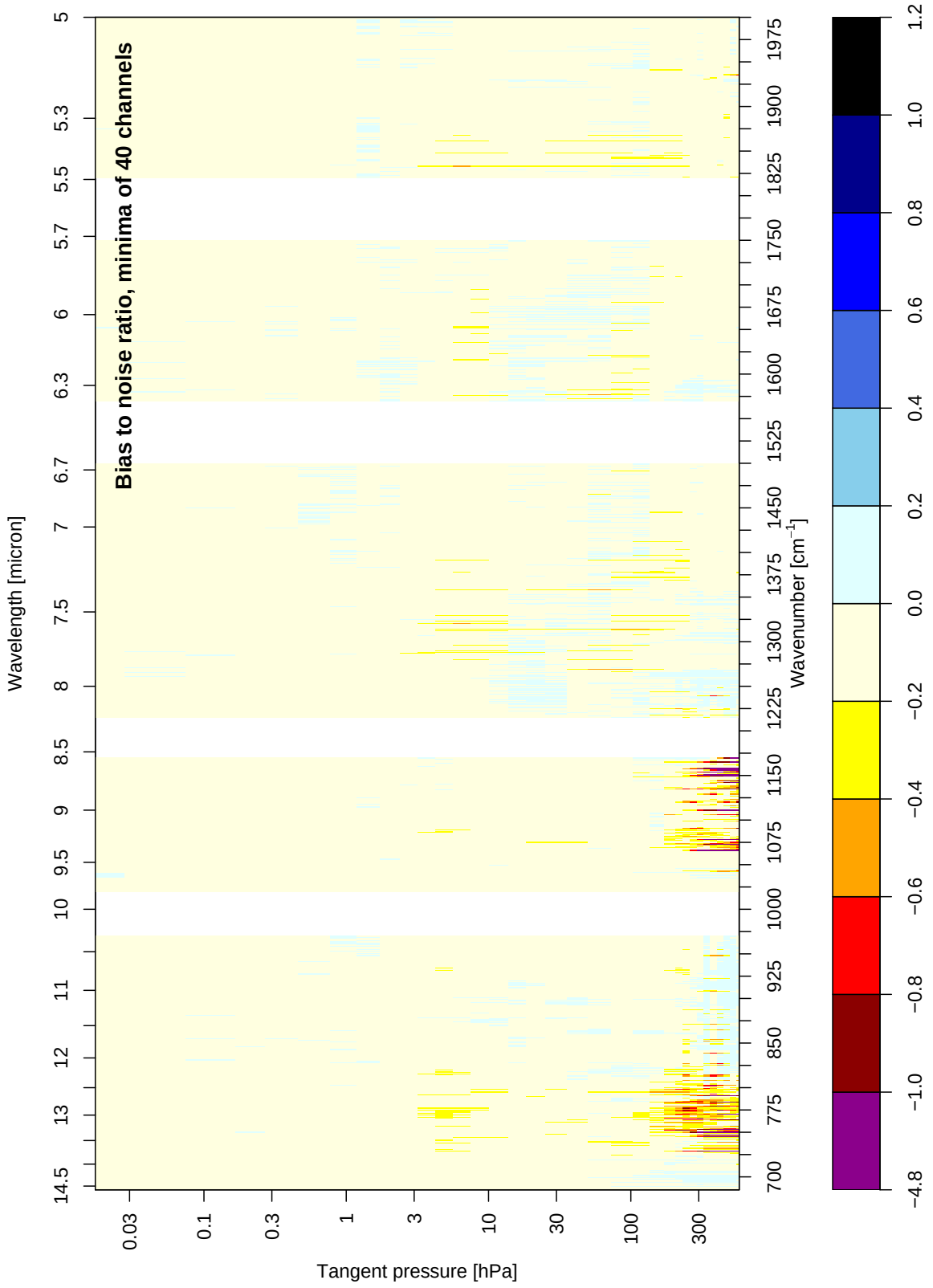

Figure 36: Mean RTMIPAS-RFM radiance differences (bias), scaled by the MIPAS noise, for the independent profile set. The plot shows the minimum of the bias to noise ratio of 40 channel intervals (i.e., 1 cm^{-1} intervals) as a function of wavenumber and pencil beam pressure.

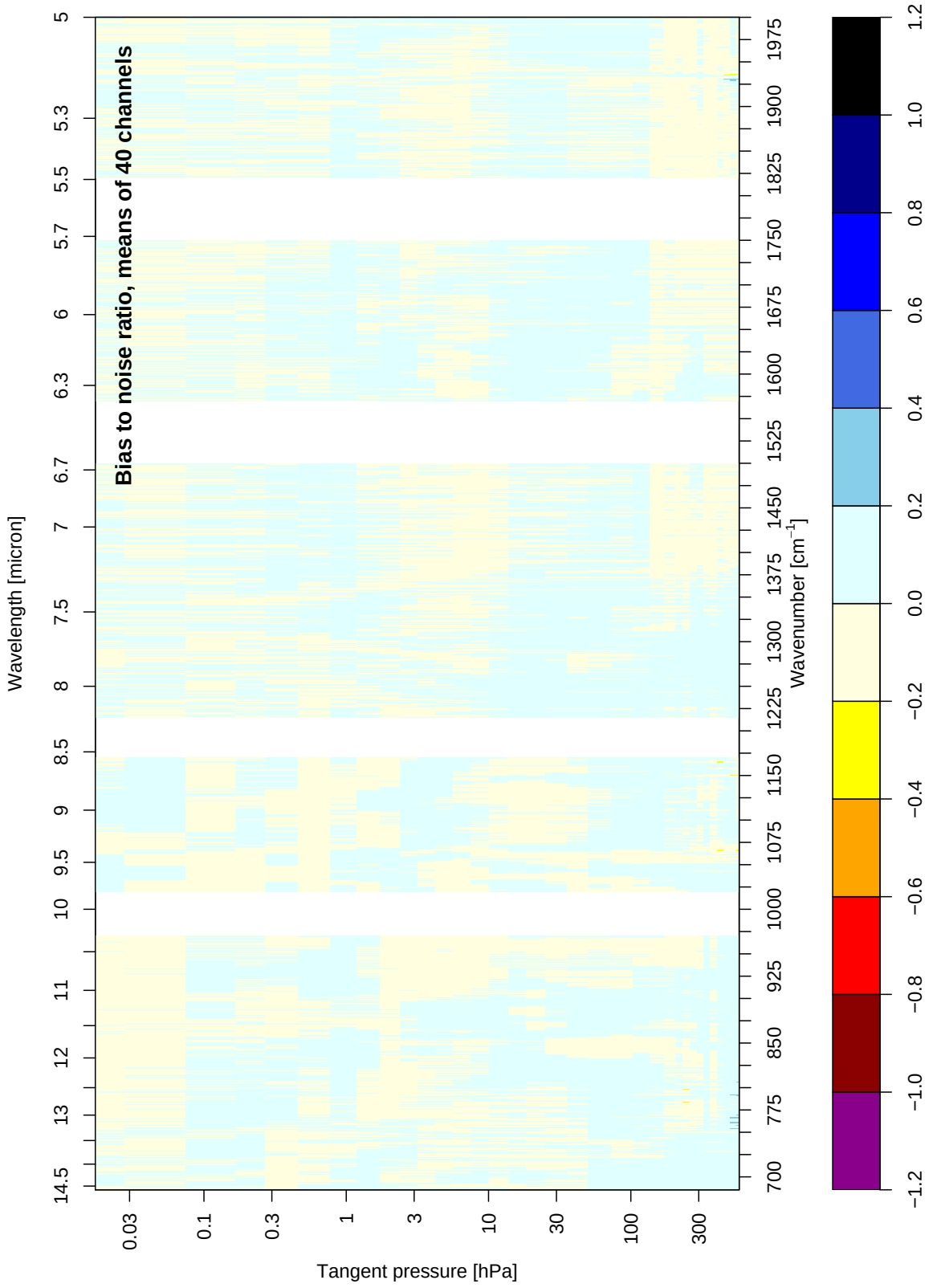

Figure 37: Mean RTMIPAS-RFM radiance differences (bias), scaled by the MIPAS noise, for the independent profile set. The plot shows the mean of the bias to noise ratio over 40 channel intervals (i.e., 1 cm^{-1} intervals) as a function of wavenumber and pencil beam pressure.

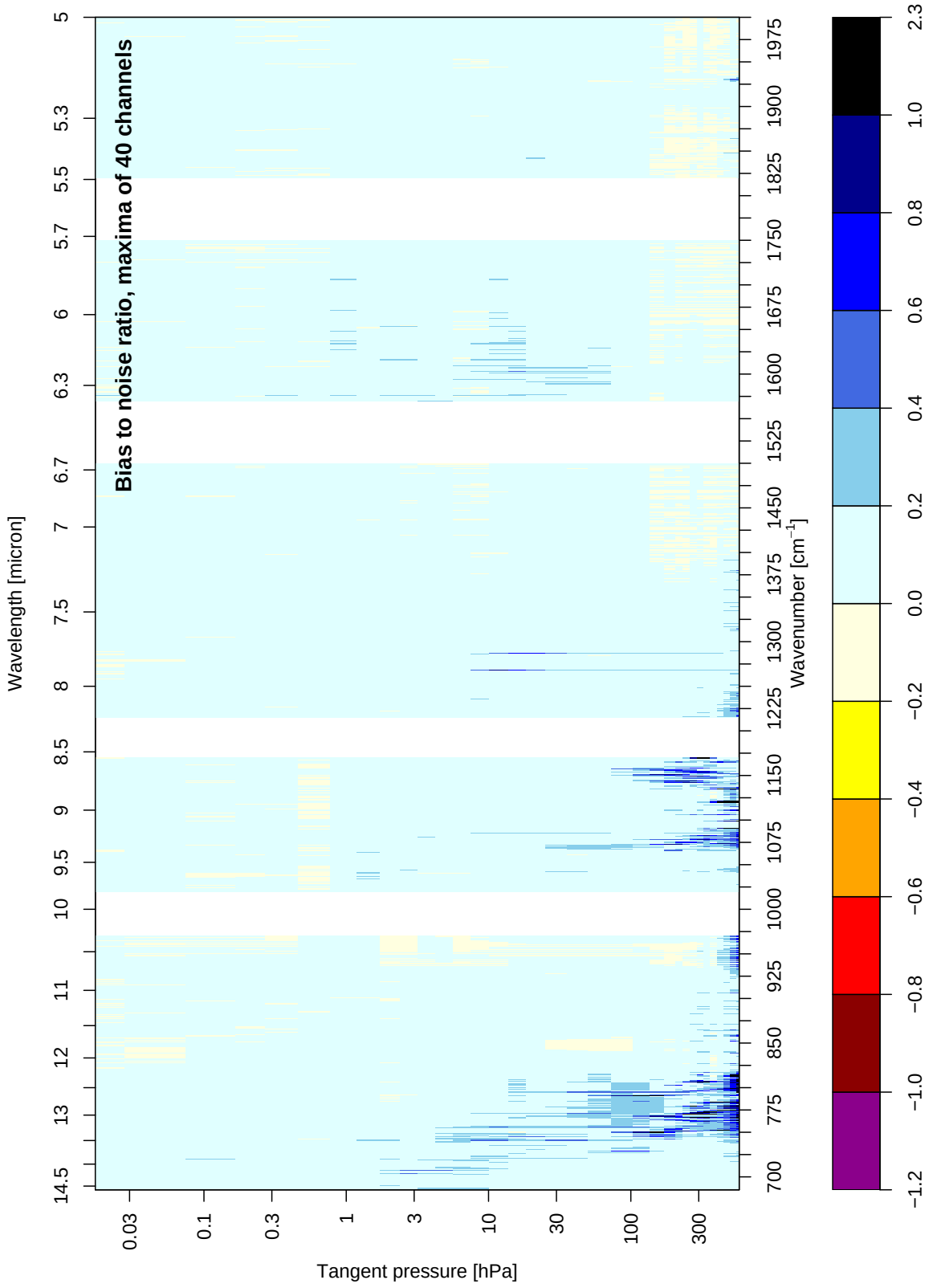

Figure 38: Mean RTMIPAS-RFM radiance differences (bias), scaled by the MIPAS noise, for the independent profile set. The plot shows the maximum of the bias to noise ratio of 40 channel intervals (i.e., 1 cm^{-1} intervals) as a function of wavenumber and pencil beam pressure.

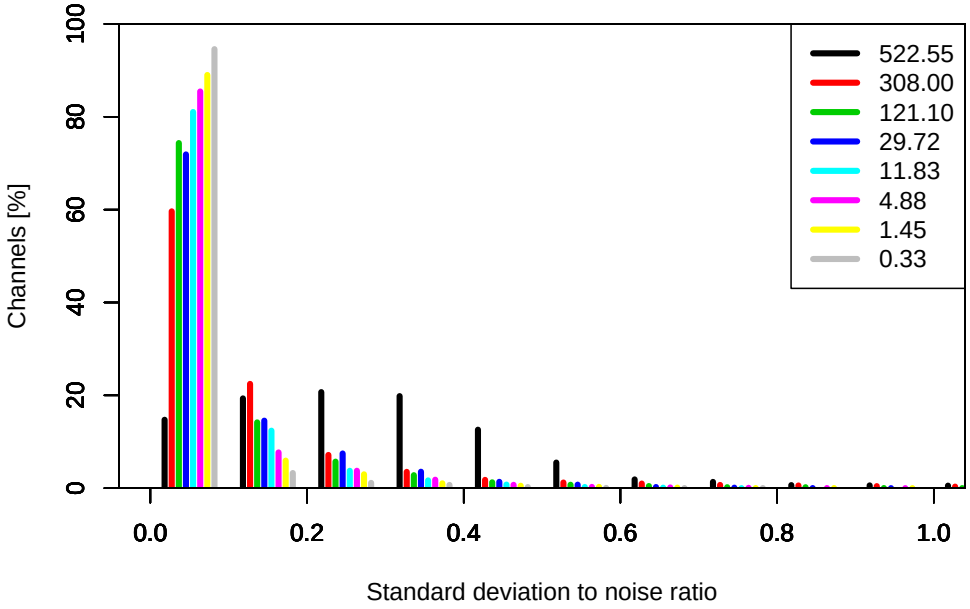

Figure 39: Distribution of the number of channels [%] in the MIPAS A-band versus the standard deviation of the RTMIPAS-RFM radiance differences, scaled by the MIPAS noise. The statistic is based on the independent profile set. Results for 8 selected pencil beams are shown, with their tangent pressures [hPa] indicated in the legend. The binning interval is 0.1.

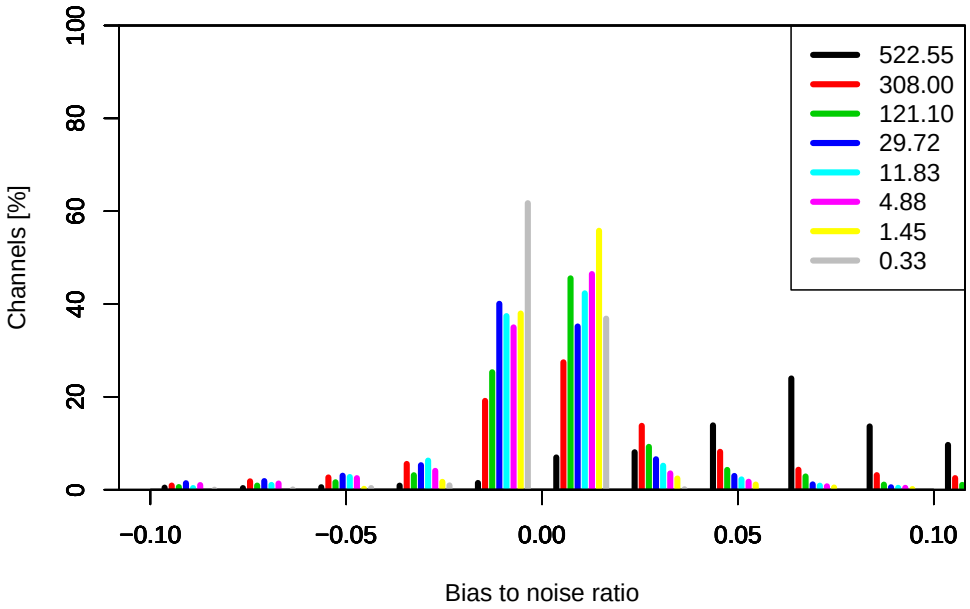

Figure 40: Distribution of the number of channels [%] in the MIPAS A-band versus the mean RTMIPAS-RFM radiance difference, scaled by the MIPAS noise. The statistic is based on the independent profile set. Results for 8 selected pencil beams are shown, with their tangent pressures [hPa] indicated in the legend. The binning interval is 0.02.

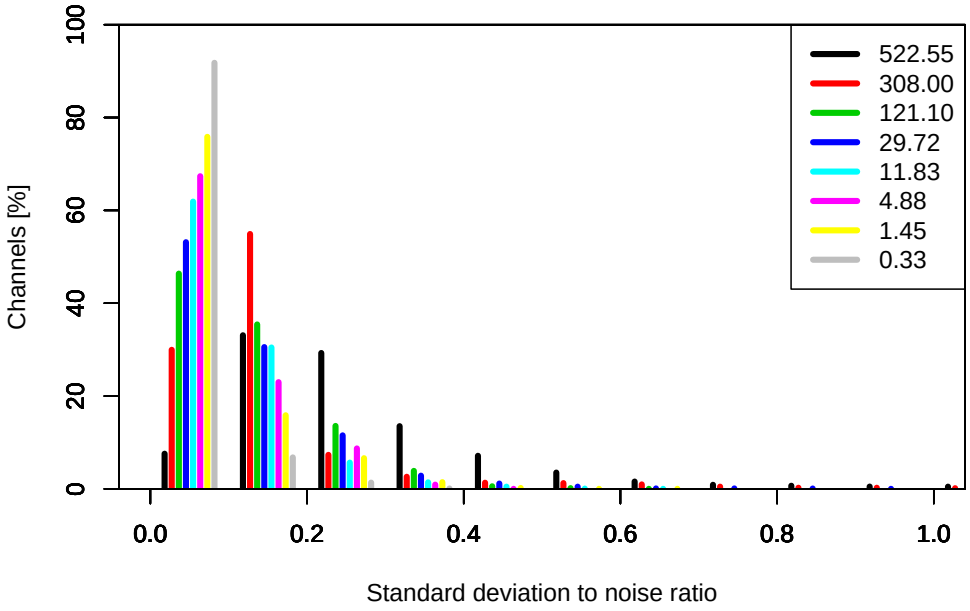

Figure 41: As Fig. 39, but for the MIPAS AB-band.

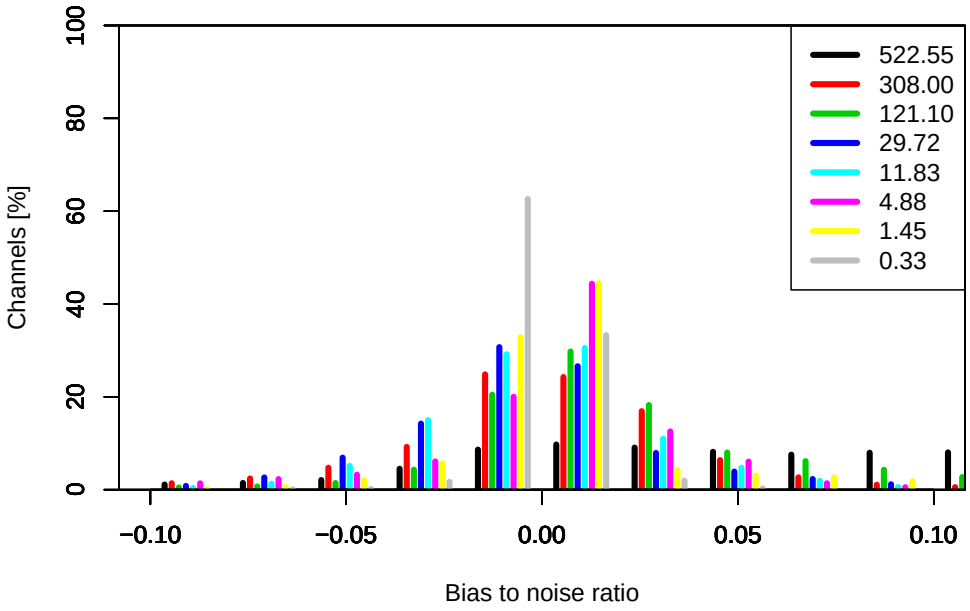

Figure 42: As Fig. 40, but for the MIPAS AB-band.

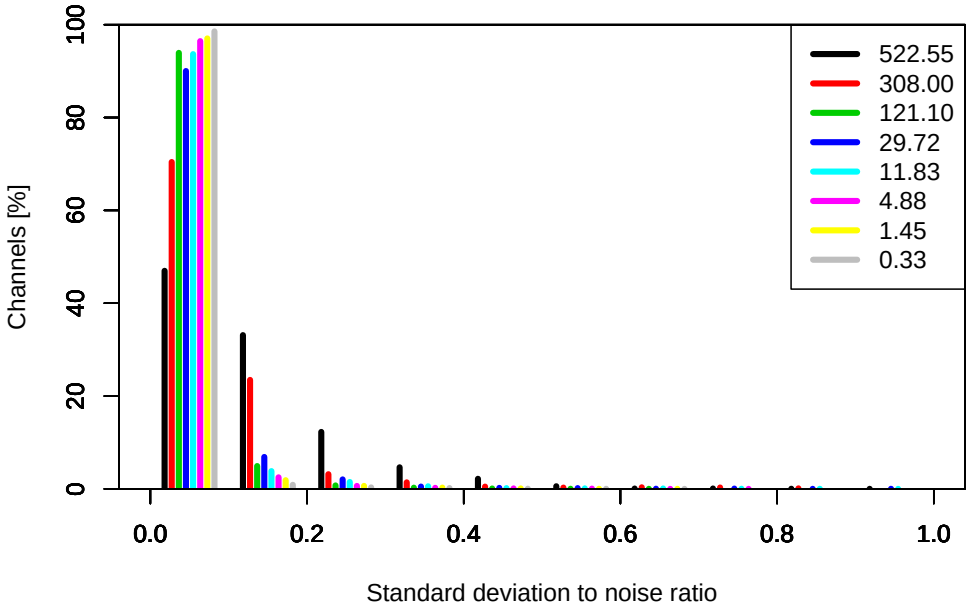

Figure 43: As Fig. 39, but for the MIPAS B-band.

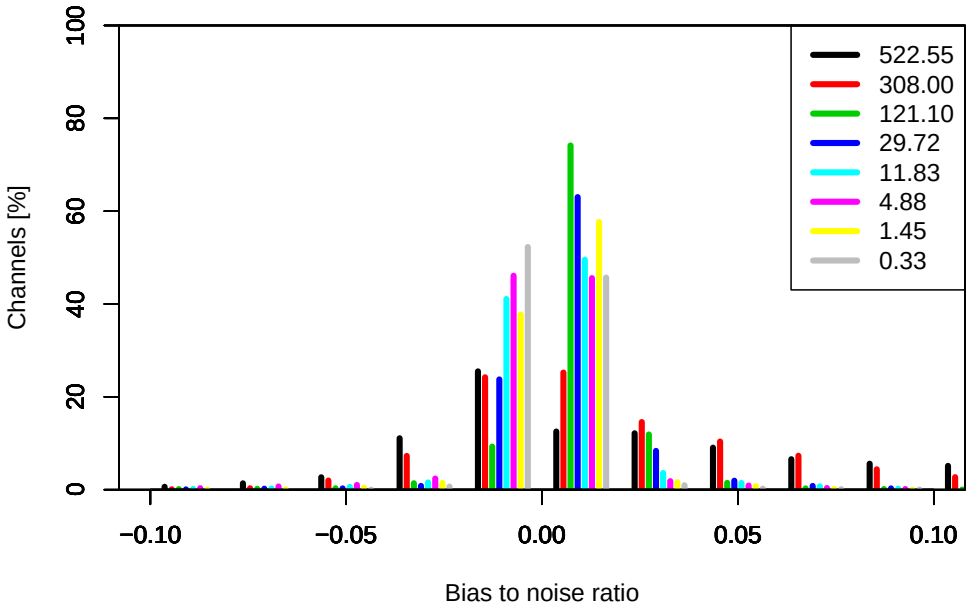

Figure 44: As Fig. 40, but for the MIPAS B-band.

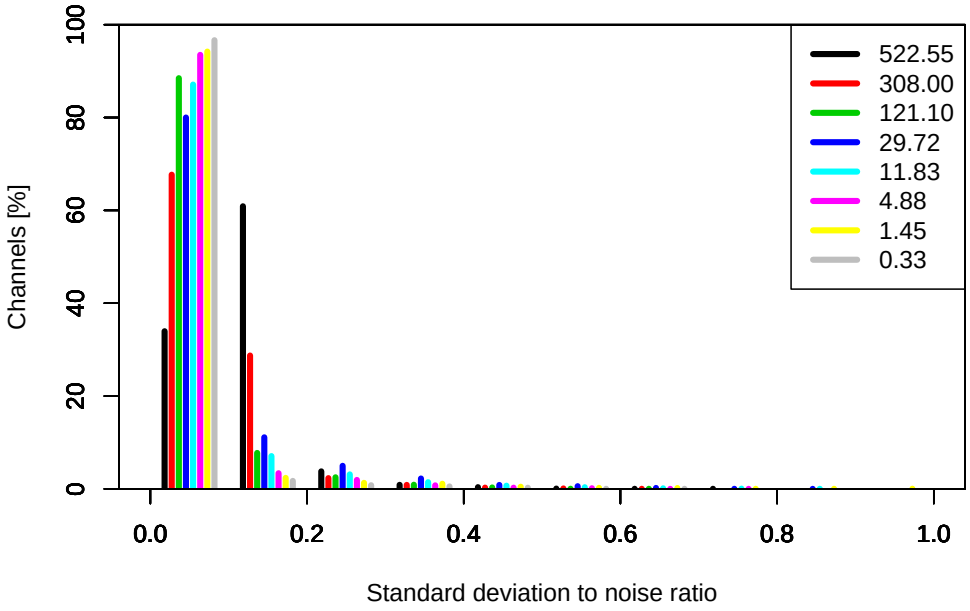

Figure 45: As Fig. 39, but for the MIPAS C-band.

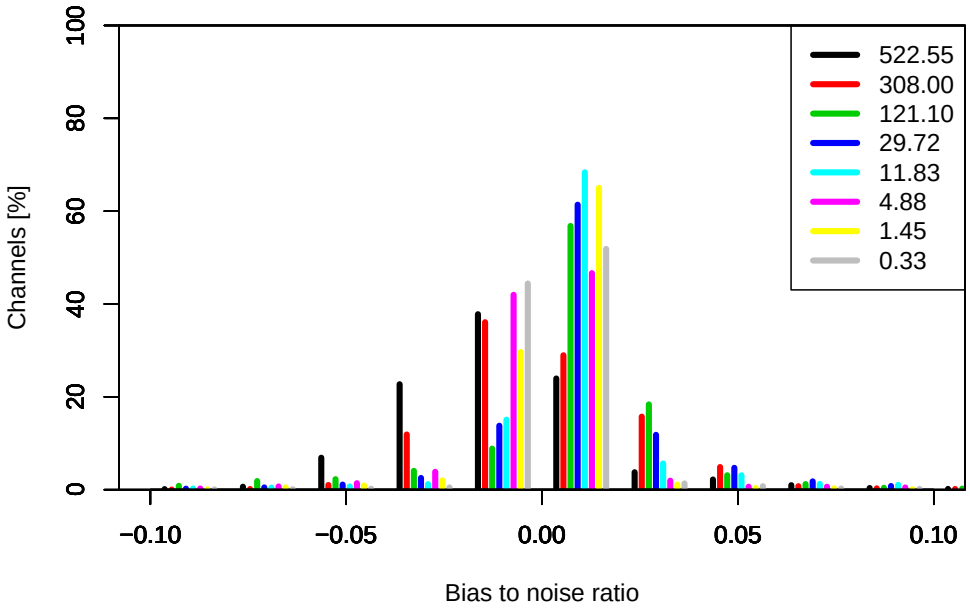

Figure 46: As Fig. 40, but for the MIPAS C-band.

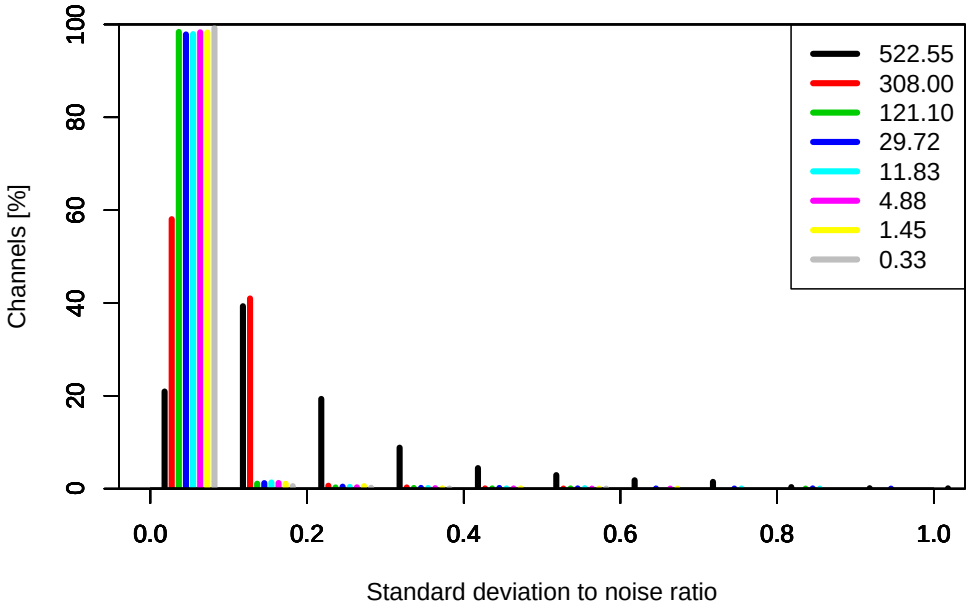

Figure 47: As Fig. 39, but for the MIPAS D-band below 2000 cm^{-1}.

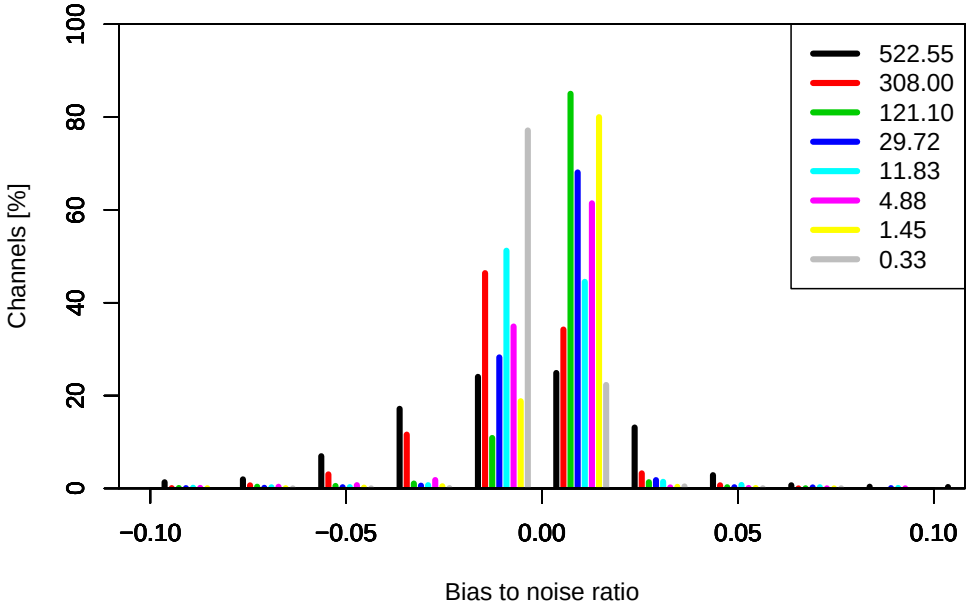

Figure 48: As Fig. 40, but for the MIPAS D-band below 2000 cm^{-1}.

4 Conclusions

This memorandum describes in detail the development and validation of a new fast radiative transfer model to compute infrared limb radiances for MIPAS (called RTMIPAS). The model has been developed with a view to assimilate limb radiances from MIPAS within the ECMWF assimilation system. It uses a fast regression-based parameterisation of convolved level-to-satellite transmittances, previously developed for nadir viewing geometry (e.g., Matricardi et al. 2004). Water vapour and ozone are treated as variable gases, whereas a climatology is assumed for all other absorbers. While in this report we have considered horizontally homogeneous atmospheres only, the method could be extended to account for horizontal gradients in the atmospheric fields with no significant loss of speed.

RTMIPAS can reproduce LBL radiances to an accuracy below the noise-level of the instrument for most spectral points and tangent heights, while offering significantly more rapid calculations compared to currently used radiative transfer methods for the limb geometry. Root mean square differences between the RTMIPAS and the RFM level-to-satellite transmittances are very small, typically around $10^{-4} - 10^{-5}$, and the maximum RMS difference rarely exceeds 0.005 for some pencil beams and channels. This good performance is comparable to that of fast radiative transfer models developed for nadir viewing, based on similar regression-based methodology (e.g., RTIASI, Matricardi 2003). The predictors used in the regression models needed to be adapted from the nadir geometry to limb viewing to achieve this performance, and the final predictor set shows considerable differences to that used in the models for nadir viewing, while the general form of the predictors is similar. The model performs similarly well for the set of training profiles taken from ERA-40 data and a quasi-independent set of profiles also sampled from ERA-40 data, suggesting that the model is suitably trained for the expected atmospheric variability.

The small errors introduced by the fast transmittance parameterisation in RTMIPAS are not going to give a significant contribution to the total forward model error, compared to uncertainties in the spectroscopy. The performance of RTMIPAS is thus expected to be adequate for data assimilation purposes. Tangent linear and adjoint routines of RTMIPAS have been developed for use in variational data assimilation.

The main advantage of RTMIPAS is that it offers very rapid calculations of MIPAS radiances: if used with the same vertical layering and the same compiling optimisations, RTMIPAS is about an order of magnitude faster than the fast version of the RFM based on irregular spectral grids and look-up-tables. In addition, the execution time needed for RTMIPAS is proportional to the number of channels, without relying on the commonly used microwindow concept, opening new possibilities for selecting channels for the assimilation from the abundance of 43,205 RTMIPAS channels. The main disadvantages of RTMIPAS are that it can handle only two variable gases (although the method could be extended) and that changes in the specification of the instrument line shape require a new derivation of the regression coefficients. The effect of the small loss in accuracy compared to the LBL model can be minimised if channels with larger "fast model errors" are avoided at the channel selection stage, using methods as described in Dudhia et al. (2002a).

RTMIPAS shows that a regression-based approach to transmittance modelling can be successfully adapted to the limb geometry, and a number of refinements to the method or extensions to other instruments are possible. As already mentioned, the model could be extended to treat other gases as variable, in addition to just water vapour and ozone, following work of Matricardi (2003) for the nadir geometry. Also, the choice of atmospheric layering could be revisited. For instance, some regression-based models for nadir viewing use levels defined by constant level-to-satellite absorber amounts rather than levels of constant pressures (e.g., McMillin et al. 1995), and this discretisation may allow larger flexibility for the choice of tangent heights used for pencil beam calculations. The experience with regression-based models for the nadir geometry suggests also that the method may be applied to other limb-sounding instruments for the infrared region (such as the High Resolution Dynamics Limb Sounder, HIRDLS), but also for the microwave region (such as the Microwave Limb Sounder,

MLS), with little or no changes to the set of predictors used. The main task to develop such a model for other instruments is the computation of a suitable transmittance database and the generation of instrument-specific regression coefficients. Choices made for the FOV convolution may also need to be revisited according to the instrument specifications. The RTMIPAS software itself is sufficiently generic to be easily adapted once regression coefficients and other specifications are provided. Further in the future, the concepts used in RTMIPAS may offer a good starting point for the development of an observation operator for combined radio occultation and active microwave limb sounding techniques, such as the planned Atmosphere and Climate Explorer (ACE)+ (Kirchengast and Høeg 2004).

Acknowledgements

Niels Bormann was funded through the ASSET project (Assimilation of Envisat Data), a shared-cost project co-funded by the Research Directorate General of the European Commission within the activities of the Environment and Sustainable Development sub-programme of the 5th Framework Programme. We thank all ASSET partners for many helpful discussions, in particular Didem Alpaslan (CNR-ISAC) for providing the MIPAS line shapes. Marco Matricardi is supported by EUMETSAT (contracts EUM/CO/01/882/DK, EUM/CO/02/989/PS), and Sean Healy is supported through the EUMETSAT/ECMWF Fellowship agreement. We are especially grateful to Anu Dudhia (Oxford University) for making the RFM available and for providing valuable support throughout this project. Frederic Chevallier (ECMWF) provided the set of diverse atmospheric profiles. Pascal Brunel (Météo France) is gratefully acknowledged for designing the RTTOV-8 code.

References

Chevallier, F., 2002: Sampled database of 60-level atmospheric profiles from the ECMWF analyses. NWP SAF Report 4, ECMWF, Reading, U.K., 27 pp.

Clough, S., F. Kneizys, and R. Davis, 1989: Line shape and the water continuum. *Atmos. Res.*, **23**, 229–241.

Cousin, C., R. Le Doucen, C. Boulet, and A. Henry, 1985: Temperature dependence of the absorption in the region beyond the 4.3 μm band head of CO_2. 2: N_2 and O_2 broadening. *Applied Optics*, **24**, 3899–3907.

Dethof, A., 2003: Assimilation of ozone retrievals from the MIPAS instrument on board ENVISAT. Technical Memorandum 428, ECMWF, Reading, UK, 19 pp.

Dudhia, A., V. Jay, and C. Rodgers, 2002a: Microwindow selection for high-spectral-resolution sounders. *Applied Optics*, **41**, 3665–3673.

Dudhia, A., P. Morris, and R. Wells, 2002b: Fast monochromatic radiative transfer calculations for limb sounding. *J. Quant. Spectrosc. Radiat. Transfer*, **74**, 745–756.

Edwards, D., 1992: GENLN2: A general line-by-line atmospheric transmittance and radiance model. Techical note TN-367+STR, NCAR, Boulder, CO, USA.

ESA, 2000: ENVISAT-MIPAS: An instrument for atmospheric chemistry and climate research. ESA report SP-1229, European Space Research and Technology Centre, Noordwijk, The Netherlands, 124 pp.

Eyre, J., 1991: A fast radiative transfer model for satellite sounding systems. Technical Memorandum 176, ECMWF, Reading, UK, 28 pp.

Eyre, J. R., G. A. Kelly, A. P. McNally, E. Andersson, and A. Persson, 1993: Assimilation of TOVS radiance information through one-dimensional variational analysis. *Quart. J. Roy. Meteor. Soc.*, **119**, 1427–1463.

Garand, L., D. Turner, M. Larocque, J. Bates, S. Boukabara, P. Brunel, F. Chevallier, G. Deblonde, R. Engelen, M. Hollingshead, D. Jackson, G. Jedlovec, J. Joiner, T. Kleespies, D. McKague, L. McMillin, J.-L. Moncet, J. Pardo, P. Rayer, E. Salathe, R. Saunders, N. Scott, P. V. Delst, and H. Woolf, 2001: Radiance and Jacobian intercomparison of radiative transfer models applied to HIRS and AMSU channels. *J. Geophys. Res.*, **106 D20**, 24,017–24,031.

Goody, R., and Y. Yung, 1995: *Atmospheric Radiation.* Oxford University Press Inc., New York, 519 pp.

Healy, S., and J. Eyre, 2003: A forward model for the assimilation of GPS radio occultation bending angle measurements. *Quart. J. Roy. Meteor. Soc.*, submitted.

Kidder, S. Q., and T. H. Vonder Haar, 1995: *Satellite Meteorology: An introduction.* Academic press, London, UK, 466 pp.

Kirchengast, G., and P. Høeg, 2004: The ACE+ mission: An Atmosphere and Climate Explorer based on GPS, GALILEO, and LEO-LEO radio occultation. In Springer Proceedings Book of OPAC-1, 1st International Workshop on Occultations for Probing Atmosphere and Climate, Graz, Austria, Sept. 2002, in press.

Le Doucen, R., C. Cousin, C. Boulet, and A. Henry, 1985: Temperature dependence of the absorption in the region beyond the 4.3 μm band head of CO_2. 1: Pure CO_2 case. *Applied Optics*, **24**, 897–906.

Marks, C. J., and C. D. Rodgers, 1993: A retrieval method for atmospheric composition from limb emission measurements. *J. Geophys. Res.*, **98 D8**, 14,939–14,953.

Matricardi, M., 2003: RTIASI-4, a new version of the ECMWF fast radiative transfer model for the infrared atmospheric sounding interferometer. Technical Memorandum 425, ECMWF, Reading, U.K., 63 pp.

Matricardi, M., F. Chevallier, and J.-N. Thépaut, 2004: An improved general fast radiative transfer model for the assimilation of radiance observations. *Quart. J. Roy. Meteor. Soc.*, **130**, 153–173.

Matricardi, M., and R. Saunders, 1999: Fast radiative transfer model for simulation of infrared atmospheric sounding interferometer radiances. *Applied Optics*, **38**, 5679–5691.

McMillin, L., L. Crone, and T. Kleespies, 1995: Atmospheric transmittance of an absorbing gas. Improvements to the OPTRAN approach. *Applied Optics*, **34**, 8396–8399.

McMillin, L., H. Fleming, and M. Hill, 1979: Atmospheric transmittance of an absorbing gas. 3: A computationally fast and accurate transmittance model for absorbing gases with variable mixing ratios. *Applied Optics*, **18**, 1600–1606.

Ridolfi, M., B. Carli, M. Carlotti, T. von Clarmann, B. Dinelli, A. Dudhia, J.-M. Flaud, M. Höpfner, P. Morris, P. Raspollini, G. Stiller, and R. Wells, 2000: Optimized forward model and retrieval scheme for MIPAS near-real-time data processing. *Applied Optics*, **39**, 1323–1340.

Rodgers, C. D., 1976: Retrieval of atmospheric temperature and composition from remote measurements of thermal radiation. *Rev. Geophys. Space Phys.*, **14**, 609–624.

Sherlock, V., 2002: Improving fast radiative transfer model predictions of water vapour line absorption. In *Technical Proceedings of the Twelfth International ATOVS Study Conference*, Lorne, Australia, International TOVS Working Group.

Simmons, A. J., and J. K. Gibson, 2000: The ERA-40 project plan. ERA-40 Project Report Series 1, ECMWF, Reading, U.K., 62 pp.

Strow, L., S. Hannon, S. DeSouza-Machado, H. Motteler, and D. Tobin, 2003: An overview of the AIRS radiative transfer model. *IEEE Trans. on Geosc. and Remote Sensing*, **41**, 303–313.

Susskind, J., J. Rosenfeld, and D. Reuter, 1983: An accurate radiative transfer model for use in the direct physical inversion of HIRS2 and MSU temperature sounding data. *J. Geophys. Res.*, **88**, 8550–8568.

Thibault, F., V. Menoux, R. Le Doucen, L. Rosenmann, J.-M. Hartmann, and C. Boulet, 1997: Infrared collision-induced absorption by O_2 near 6.4μm for atmospheric applications: measurements and empirical modelling. *Applied Optics*, **36**, 563–567.

Venables, W., and B. Ripley, 2002: *Modern Applied Statistics with S.* Springer, New York, 495 pp.

von Clarmann, T., M. Höpfner, B. Funke, M. López-Puertas, A. Dudhia, V. Jay, F. Schreier, M. Ridolfi, S. Ceccherini, B. Kerridge, J. Reburn, and R. Siddans, 2003: Modelling of atmospheric mid-infrared radiative transfer: the AMIL2DA algorithm intercomparison experiment. *J. Quant. Spectrosc. Radiat. Transfer*, **78**, 381–407, doi:10.1016/S0022–4073(02)00262–5.